REVIEW

Check for updates

Ferroelectric polarization in 2D halide hybrid perovskites: influence on bulk crystals, thin films, and applications

Raja Sekhar Muddam and Lethy Krishnan Jagadamma ⓘD *

Ferroelectric materials undergo spontaneous polarization that can be reversed by applying an external electric field. This property plays the most important role in applications such as logic gates, microwave communications, piezo energy harvesting, memory storage such as ferroelectric random-access memory (FeRAM), and ferroelectric sensors and actuators. Recently, hybrid halide perovskites (HHPs) have started demonstrating impressive ferroelectric properties in addition to their excellent photovoltaic performance. Compared to traditional oxide perovskites and organic ferroelectric materials, HHPs have the advantage that they can be simple solution-processed yet with immaculate crystal quality which is suitable for realizing next-generation thin film flexible electronics and FeRAM in neuromorphic computing. This review focuses on the current status of ferroelectric properties of two-dimensional (2D) halide perovskite single crystals and covers the limited reports available on thin film HHPs. Furthermore, we explain the challenges in the ferroelectric characterization of thin film HHPs and compare them with those of single crystals.

1. Introduction

Spontaneous electric polarization reversed by an external electric field is a unique feature of a ferroelectric material, which plays the most important role in many related advanced applications such as piezo energy harvesting, ferroelectric random access memory (FeRAM), and ferroelectric sensors.[1] Thin film ferroelectrics are indispensable in modern technology due to their versatility and ability to be integrated into a wide range of applications, from electronics to energy harvesting and beyond.[2] Thin film ferroelectrics promise excellent mechanical flexibility when compared to bulk materials and can be engineered with specified properties based on their composition and thickness.[3,4] These attributes are important for non-volatile memory devices and effective energy-harvesting system applications.[5] Even though inorganic ferroelectric materials like lead zirconate titanate (PZT) & barium titanate (BATiO₃) show superior ferroelectric properties with high saturation polarization (P_s) 20 to 70 & 25 μC cm^{-2}, respectively,[6,7] these materials have some drawbacks such as rigidity, high processing temperature greater than 1000 °C, and difficulties in integrating with modern flexible electronics. Although the so-called organic ferroelectrics, such as polyvinylidene fluoride

(PVDF) and its copolymers, are more flexible and require lower processing temperature (below ∼200 °C) these materials typically have very low polarization (PVDF = 0.13 μC cm^{-2})[6] values and have inherently higher environmental instability. Thus both families of existing ferroelectric materials suffer from scalability issues and fall short in certain aspects when it comes to satisfying the demands of advanced ferroelectric applications like self-powered flexible electronics & FeRAM in neuromorphic computing.[7] Thus there is a strong demand for a novel family of ferroelectric materials with excellent polarization properties and yet capable of being integrated with modern technological advancements.[8]

Recently, hybrid halide perovskites (HHPs) have emerged as promising ferroelectric materials in addition to their photovoltaic performance. Originally, HHPs were widely investigated mostly for their potential in photovoltaic applications, where they have shown exceptional power conversion efficiencies (27%, most recent certified value) within a decade since their inception in 2009. These materials have superior light absorption and charge-transporting properties and can be processed using simple solution processing methods.[9,10] Over time, researchers have discovered their potential in other fields, including light-emitting diodes, lasers, photodetectors, and more recently, ferroelectric applications.[11] The presence of additional ferroelectric behavior in the HHPs makes these materials to be explored in other energy harvesting applications such as piezoelectric energy harvesting and in technological

Energy Harvesting Research Group, School of Physics & Astronomy, SUPA,
University of St Andrews, North Haugh, St Andrews, Fife KY16 9SS, UK.
E-mail: lkj2@st-andrews.ac.uk

applications such as FeRAMs. Exploring the ferroelectric behaviour in HHPs would unravel the fundamental properties of these materials related to ferroelectricity, and will provide novel insights into the dynamic properties of the organic cation molecules. In addition, ferroelectric behaviour in HHPs gives a detailed understanding of the charge carrier dynamics in highly efficient photovoltaics and can even improve the photovoltaic properties due to efficient charge separation and extraction. From a technology point of view, ferroelectric HHPs enable applications in non-volatile memory, logic gates, sensors, actuators, piezo energy harvesters, and reconfigurable optoelectronic devices.[5] The HHPs' structural phase stability issues are due to their easy ion migration and environmental sensitivity (humidity and UV-induced degradation). However, researchers are actively exploring strategies such as surface passivation and encapsulation to stabilize these materials.[12] Among these different promising properties, ferroelectricity has received tremendous attention because of its ease of synthesis and tunable ferroelectric properties.[13] HHPs exhibit distinguishing dielectric properties, Curie temperatures well above room temperatures (such as 200 °C) and notable piezoelectric responses.[14,15] Thus, HHPs with exceptional ferroelectric performance can have significant opportunities in advanced applications in next-generation ultra-high density data storage, energy harvesting, memory devices and high-speed data communications.

Ferroelectricity in 2-dimensional (2D) single crystal lead halide perovskites was reported for the first time in 2015 in (benzylammonium)$_2$PbCl$_4$ by Heng-Yun Ye et al., using the Sawyer–Tower ferroelectric tester & piezoresponse force microscopy (PFM),[16] and this has opened up an entirely new avenue for this field.[17] Single crystals contain fewer defects and grain boundaries than polycrystalline thin film structures, leading to better ferroelectric properties.[2] Single crystal halide perovskites demonstrated higher dielectric constants, superior polarization stability, and more excellent charge carrier mobility compared to their thin film counterparts.[18,19] Some single crystal HHPs are (ATHP)$_2$PbBr$_4$ (ATHP = 4-aminotetrahydropyran), (BA)$_2$CsPb$_2$Br$_7$ (BA = butylammonium), and [(R)-N-(1-phenylethyl)ethane-1,2-diaminium]PbI$_4$. These materials have a dielectric constant (ε_r) of 13, 37, and 10, and saturation polarizations (P_s) of 5.6, 4.2 & 0.15 μC cm^{-2} respectively.[20–22] Halide perovskite thin films offer a number of beneficial properties compared to single crystals, especially in piezoelectric and ferroelectric applications. On the one hand, thin films are flexible and can be easily integrated into a wide range of device architectures, which is vital for the Internet of Things (IoT) applications as these technologies require ultra-lightweight, compact and portable power sources, energy storage, memory devices and associated electronic devices for innumerable data transmission and reception.[5,23,24] Although single crystal halide perovskites showcase most of the attractive features, they are accompanied by several roadblocks constraining their practical applications, such as the synthesis of large-area single crystals with uniform properties, and is a longstanding challenge.[3] Moreover, single-crystal ferroelectric HHPs are mechanically brittle and environment-sensitive, and it is

challenging to integrate these ferroelectric HHP single crystals with advanced electronic components. However, thin film HHPs have several advantages such as mass-scale fabrication, low material consumption, cost-effective simple solution processing and tunable ferroelectricity. Despite these advantages, polycrystalline ferroelectric thin films face several challenges in comparison to single-crystal ferroelectrics, such as defects and grain boundaries, which can severely affect the electrical and ferroelectric polarisation properties.[25] Strategies to control the ferroelectric behaviour in thin films include compositional engineering for optimal perovskite structures, surface passivation during fabrication steps for low defect density, and interface modulation providing a band alignment suitable for charge transport; these are well-known and used techniques in photovoltaics.[26–28] Furthermore, the advancement in deposition methods, e.g., spin coating, blade coating, and thermal evaporation, has allowed us to obtain high-quality thin films with great ferroelectric properties.[29–31] In this review, we will compare and discuss the ferroelectric properties of halide perovskite single crystals and thin films with an emphasis on 2D halide perovskites to provide a guideline in identifying the properties that are particularly interesting in realising next-generation energy harvesters and memory devices.

2. Ferroelectricity

Ferroelectric materials show spontaneous polarization, which can switch/reverse under an external electric field. The presence of a finite polarisation at zero electric field and the direction reversal of the polarisation vector are the distinct features of ferroelectrics over piezoelectric materials. In a ferroelectric material, the regions of uniform electric dipole alignment (polarisation) are known as domains. The interface between the two domains is called domain walls. These domain walls are usually very thin and only a few lattices thick. The direction of polarisation will be different in adjacent domains, and the net polarisation of the specimen remains zero when no electric field is applied.[32] Fig. 1a shows the random alignment of dipoles/net polarisation in a multidomain grain. A ferroelectric crystal usually possesses a multidomain structure and when a strong electric field is applied such that the direction of the field is opposite to the direction of polarisation of a domain, the spontaneous polarisation of the domain reverses. This dynamic process of domain reversal is called ferroelectric switching as shown in Fig. 1b. This ferroelectric domain switching depends on two factors such as the applied electric field and temperature.

Polarisation P is defined as the dipole moment (p) per unit volume.[36]

$$P = \frac{p}{\text{total volume}} \tag{1}$$

The dipole moment is defined as $\vec{p} = \int dV \rho(\vec{r}) \vec{r}$ (2)

where $\rho(\vec{r})$ is the charge density in the molecule over the volume

This journal is © The Royal Society of Chemistry 2025

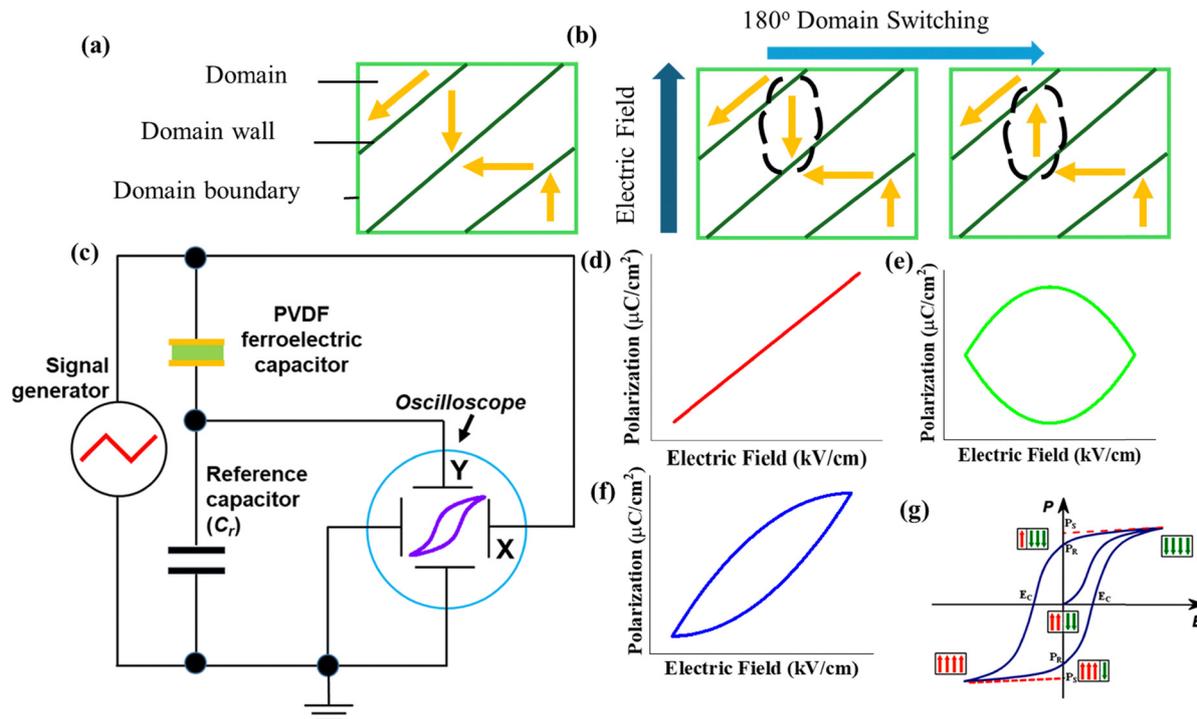J. Mater. Chem. C, 2025, 13, 10488–10506 | 10489

Fig. 1 (a) Multidomain in a ferroelectric crystal, (b) domain switching in a ferroelectric crystal due to an external field, and (c) internal schematic of the Sawyer–Tower circuit. Reproduced from ref. 33 with permission from Springer Nature, copyright 2019. P–E hysteresis loop plot of ref. 33 (d) ideal linear capacitor, (e) ideal resistor, (f) lossy capacitor,[34] and (g) non-linear ferroelectric device. Reproduced from ref. 35 with permission from Springer Nature, copyright 2019.

dV. As the temperature increases, the bulk polarisation value decreases, and the material changes from a ferroelectric to a paraelectric phase. This temperature where this transition happens (lower symmetry to higher symmetry phase) is called the Curie temperature (T_C).

Ferroelectric materials are characterized by their nonlinear polarisation (P) with respect to the external electric field (E) and hysteresis of the P–E loop as well. The Sawyer–Tower method is the most widely known technique for measuring the P–E properties of ferroelectric materials where an alternating electric field polarises a ferroelectric sample, and its polarization is measured *via* the build-up of charge on a reference capacitor, as shown in Fig. 1c. The Sawyer–Tower circuit is unique because it directly measures the charge displacement.

$$\text{Polarization } (P) \text{ is a function of } U_0 C_0/S \qquad (3)$$

where U_0 is the voltage on a measured sample, C_0 is standard capacitance, and S is the sample's surface area.

The method developed by Sawyer and Tower is simple to implement and can measure many types of ferroelectric samples, such as ceramics, and thin films, as well as innovative new materials like halide hybrid perovskites thin films.[33]

In the case of an ideal capacitor, the polarization varies linearly with the electric field, as shown in Fig. 1d; this is because voltage lags 90° by current, which results in charge and voltages being in phase. In an ideal resistor, the current is in phase with the voltage, and the resulting P–E loop is in a circle from the centre, as shown in Fig. 1e. The lossy capacitor's (the

parallel combination of an ideal capacitor and linear resistor) P–E loop is shown in Fig. 1f. Here, the area under the loop is due to the loss tangent of the device, and this loss may be due to the leakage current or dielectric hysteresis, and its slope is proportional to the capacitance.[34] Fig. 1g shows the P–E loop of ferroelectric materials; at $E = 0$ (origin), the sum of + and − dipoles is equal, which is electrically neutral. At = $\pm E_{max}$, all the dipoles are aligned in one direction, and here we can see that maximum spontaneous polarisation is due to the sum of all polarizations in the material, such as electronic, ionic, and interfacial charges. These different types of dipole charges again depend on the excited frequency range; at higher frequency ($>$1 M Hz), ionic and space charge polarization is not significant.[37] After the electric field sweeps from E_{max} to zero, we can still see the polarization at $E = 0$, which is remnant polarization in the material. The electric field where the polarization value reaches zero and polarisation switching happens is called the coercive field, denoted as E_C.

The ferroelectric properties of HHPs are controlled by the type of crystal structure, dielectric properties, Curie–Weiss behaviour, and type of polarisation mechanism. The crystal structure of the ferroelectric materials should be a polar, non-centrosymmetric phase. Among 32 crystal point groups, only 10 polar point groups show ferroelectric properties ($P1$, $P2$, Pm, $Pmm2$, $Pmc2_1$, $Pna2_1$, $P4mm$, $P4nc$, $P3$, and $R3m$).[38] In addition to that, one more parameter is the dielectric constant, which determines the strength of the dipole moment. A higher dielectric constant enhances dipole interactions, strengthening

10490 | *J. Mater. Chem. C*, 2025, **13**, 10488–10506

This journal is © The Royal Society of Chemistry 2025

ferroelectric behaviour. Consequently, the material exhibits anisotropic dielectric behaviour, where the dielectric constant varies with the direction, influencing polarization. Ferroelectric properties manifest below the Curie temperature, while above this temperature, the material transitions to a non-ferroelectric phase. The Curie–Weiss law describes the relationship between the Curie temperature and the dielectric constant. Eqn (4) describes this relationship.[39]

$$\epsilon_r = \frac{C}{T - T_C} \qquad (4)$$

where ϵ_r is the relative dielectric constant, T_C & T are Curie & absolute temperatures, and C is a Curie constant. For the temperature (T) below T_C, all the ferroelectric domains align in one direction, which strengthens and creates a net spontaneous polarisation in the material. When T is near T_C, all the dipoles are aligned easily, and it causes a sharp increment in the dielectric constant. The ferroelectric response involves various mechanisms such as displacive, geometric (tilting), order–disorder, and hydrogen bonding mechanisms depending on the direction of poling and polarization, which mainly depends on the type of material.[40]

3. Background of ferroelectric hybrid halide perovskites

3.1 Structure and composition of HHPs

HHPs are a class of materials with the formula ABX_3, where typically A is an organic cation such as methylammonium ($MA^+ = CH_3NH_3^+$) or formamidinium [$FA^+ = HC(NH_2)_2^+$], methylhydrazinium ($MHy^+ = CH_3NH_2NH_2^+$)[41,42] and aziridinium ($AZR^+ = C_2H_6N^+$),[43,44] B is a metal cation such as Pb^{2+}, Sn^{2+}, *etc.*, and X is a halide ion like I^-, Br^-, Cl^-. In the lattice structure of HHPs, as depicted by a cubic lattice in Fig. 2a, the metal cation B and halide group X form an octahedral BX_6 cage, and the larger-sized organic cation A covers all corners of this BX_6 cage. The 2D HHPs are layered materials where one inorganic octahedral cage (BX_6) is sandwiched with two organic spacers, as shown in Fig. 2b. The general formula is $(A')_2(A)_{n-1}B_nX_{3n+1}$, where A′ is a bulky organic cation, A is a small organic cation, B is a metal cation, and X is a halide anion.[45] It begins as a single layer ($n = 1$) and then gradually thickens with quasi 2D structures at $n = 2$ to 4, followed by the 3D structure (ABX_3) for larger values of $n = \infty$. Fig. 2c shows how this 2D perovskite
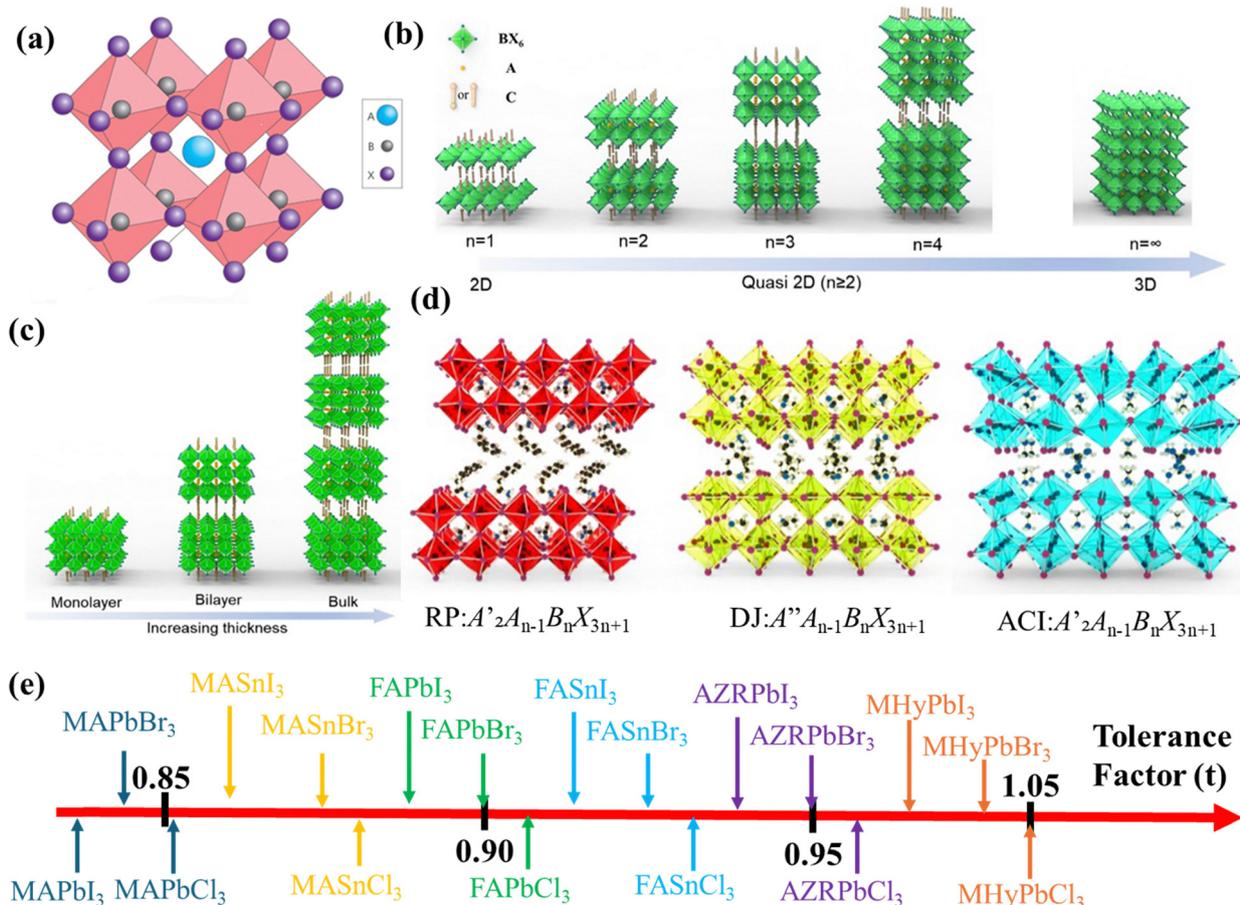

Fig. 2 (a) The typical three-dimensional (3D) crystal structure of metal–halide perovskites with the general formula ABX_3. Reproduced from ref. 54 with permission from Springer Nature, copyright 2014. (b) The transition from 2D to 3D perovskites, (c) 2D perovskite structures evolve as they increase in layer thickness. (d) Comparison of different types of quasi-2D crystal structures for $n = 3$. Reproduced from ref. 55 with permission from Springer Nature, copyright 2021. (e) Tolerance factor variation with different halide hybrid perovskite compositions.[37]

This journal is © The Royal Society of Chemistry 2025

J. Mater. Chem. C, 2025, **13**, 10488–10506 | **10491**

structure changes from a monolayer to bilayers and eventually to the bulk phase with an increase in thickness. This change significantly affects the charge transport and defect density of the perovskite, which in turn influence the electrical and optical properties of the material. Fig. 2d illustrates different phases of the quasi-2D crystal structures, which are Ruddlesden–Popper (RP), Dion–Jacobson (DJ), and alternating cations in the interlayer space (ACI) perovskites. These 3 structures have a different stacking of the organic and inorganic layers' connectivity. In the RP phase, a large monovalent organic cation separates the inorganic layers with weak interlayer van der Waals forces. However, in some special cases like RP-$(MHy)_2PbBr_4$ perovskites, van der Waals forces are eliminated due to multiple strong interactions of the hydrogen bonds in between the inorganic layers. In $(MHy)_2PbBr_4$ perovskites, the interlayer distance is very small (8.91 Å at 300 K), which leads to strong interaction in inorganic $(PbBr_4)$ layers, resulting in cancelling out the van der Waals forces.[46] In the case of DJ, a stronger hydrogen bonding exists between the inorganic layers and diammonium cations. The ACI structure comprises two cations in the interlayer space, for instance, guanidinium (GA^+) and MA^+ in $(GA)(MA)_nPb_nI_{3n+1}$,[47] imidazolium (IM^+) and MHy^+ in $IMMHyPbX_4$[48] or IM^+ and 1,2,4-triazolium (Tz) in $IMTzPbBr_4$,[49] which helps stabilize this phase with a reduction in charge carrier recombination sites.[50] Most of the previously reported ferroelectric single-crystal HHP materials have a RP structure phase as shown in Table 1. Because this phase has a higher asymmetric crystal orientation, it results in enhancing the dipole moment. The tuning of the polarisation properties of HHPs provides pathways for designing them for different ferroelectric applications, such as non-volatile memory and piezo energy devices. In addition to the above 2D HHP crystal structures, hexagonal HHP crystal structure is another new dimensionality in the 2D HHP category. The crystal structure of hexagonal 2D HHPs' general formula is $A_2B_nX_{3n+1}$, and here, inorganic layers are coupled with face-sharing or edge-sharing connectivity. In addition, this structure has denser packing than RP, DJ, and ACI 2D crystal structures.[51] The 2D hexagonal crystal structure has limited charge flow in the face-sharing inorganic crystal connectivity.[52,53]

The change of inorganic and organic ion sizes and tilting of the BX_6 octahedral unit depend on the tolerance factor.[82]

$$t = \frac{r_A + r_X}{\sqrt{2}(r_B + r_X)} \quad (5)$$

where r_A, r_B, and r_X represent the radii of the A, B, and X ions, respectively, and the ferroelectric properties of HHP materials highly depend on the A, B, and X radii. The above tolerance factor is mainly considered for the 3D-ABX_3 structure. If the HHPs are in a 2D phase $(A')_2(A)_{n-1}B_nX_{3n+1}$, then A organic radius is considered as r_{Aeff}. The above Goldschmidt's tolerance equation is converted to a form shown in eqn (6).[83,84]

$$t = \frac{r_{Aeff} + r_X}{\sqrt{2}(r_B + r_X)} \quad (6)$$

Similarly, a 2D-double halide hybrid perovskite Goldschmidt's

tolerance factor equation is modified as shown in eqn (7); here, h_{Xeff} is the X-anions' effective height.[85]

$$t = \frac{r_{Aeff} + r_X}{\sqrt{2}(r_B + 0.5h_{Xeff})} \quad (7)$$

Fig. 2e shows the tolerance factor variation for different HHP molecules with organic, inorganic, and halide ion variations. In this case, $MHyPbI_3$ (methylhydrazinium lead iodide) is predicted to have a higher tolerance factor than $AZRPbI_3$ (aziridinium lead iodide), $FAPbI_3$ (formamidinium lead iodide) & $MAPbI_3$ (methylammonium lead iodide) mainly due to the larger ionic radius of the MHy^+ (0.26 nm)[43,86] cation compared to AZR^+ (0.23 nm),[87] FA^+ (0.19–0.22 nm),[37,54] and MA^+ (0.18 nm).[54] Generally, the lower dimensional (2D, 1D) HHP tolerance factor is higher than the 3D structures due to its bulky organic cations in the A site.[88,89] S. Burger and group reviewed the current state of the art of HHP tolerance factors; the authors explained the impact of tolerance factors on phase stability and their role in dimensionality variation.[90] This larger tolerance factor could form a stabilized perovskite structure. Since the Cl atom is smaller than the Br and I atoms, the tolerance factor of $FASnCl_3$ is larger than that of $FASnI_3$. Modifying the halide component (e.g., changing I to Br or Cl) will modify the bandgap and lattice parameters of the perovskite structure, which can affect its ferroelectric behaviour. Tighter lattice structures (smaller ions like Cl^-) can promote ferroelectric behaviour because of enhanced ionic polarization. Different anionic frameworks (like Pb, Sn, or mixed anions) could fine-tune the perovskite's electronic environment, thereby influencing their ferroelectric behavior.[91]

3.2 Ferroelectricity in HHPs

The motion of organic cations with a large dipole moment in the metal halide cavity gives rise to unusual electrical properties in hybrid perovskites. This dipole moment (μ) is related to the symmetry of the organic cation such as μMHy (2.80 D) > μMA (2.26 D) $\gg$ μFA (0.22 D) > $\mu GA = 0$.[92,93] Based on the symmetry, the hybrid perovskites can be classified as centrosymmetric, asymmetric, and non-centrosymmetric. Moreover, the degree of non-centrosymmetry can be tuned by applying an external stimulus of heat, electric field, photon energy, stress, etc.[94] The orthorhombic structure of mixed halide perovskite $[MAPb(Br_{0.5}I_{0.5})_3]$ changes its space group from centrosymmetric $(P2_1/m)$ to noncentrosymmetric (Pm) under light illumination as shown in Fig. 3a.[95] This tuning of non-centrosymmetry gives rise to many interesting properties of piezoelectric, pyroelectric, and high switchable dielectric constants. In the past decade, many conflicts have existed regarding the origin of ferroelectricity in 3D-HHP materials, especially in the case of $MAPbI_3$, where most of the materials are centrosymmetric crystals.[96] In contrast, bulky organic cations and inorganic moieties in 2D HHPs, which are easily coupled with order and disorder transitions of the organic cations, lead to spontaneous polarization. The dynamic motion of the organic cation drives the ferroelectricity in the 2D HHPs. In addition to that, the lattice distortion and displacive ions in the

10492 | *J. Mater. Chem. C*, 2025, **13**, 10488–10506

This journal is © The Royal Society of Chemistry 2025

Table 1 Ferroelectric properties of lead based 2D single crystal HHPs

Chemical formula	Polarization ($\mu C\ cm^{-2}$) at temperature (K)	Coercive field ($kV\ cm^{-1}$)	Crystal structure	Curie temperature (K)	Ref.
2D-single layered Ruddlesden–Popper (RP)					
$(CPA)_2PbCl_4$ (CPA = 3-chloropropylammonium)	2.1 at 350	0.4	Orthorhombic ($Cmc2_1$)	360	56
$(ATHP)_2PbBr_4$ (ATHP = 4-aminotetrahydropyran)	5.6 at 363	40	Orthorhombic ($Cmc2_1$)	503	57
$(4,4\text{-}DFHHA)_2PbI_4$ (4,4-DFHHA = 4,4-difluorohexahydroazepine)	1.1 at 293	545	Orthorhombic ($Cmca$)	454	15
$(CHA)_2PbBr_{4-4x}J_{4x}$ (x = 0–1)	x = 0, 0.1125, and 0.175 are 5.8, 8.5, and 7.5 at 298	x = 0, 0.1125, and 0.175 are 22, 12 and 16	Orthorhombic, $Cmc2_1$ for x = 0, 0.1125 and 0.175	383 K for x = 0 393 K for x = 0.1125 393 K for x = 0.1125	58
(CHA = cyclohexylammonium)					
$(C_4H_9NH_3)_2PbCl_4$	2.1 at 300	14.3	Orthorhombic ($Cmc2_1$)	328	59
$[\text{2-Fluorobenzylammonium}]_2PbCl_4$	5.35	17	Orthorhombic ($Cmc2_1$)	448	60
$[(CH_3)_2CHCH_2NH_3]_2PbCl_4$	4.8 at 293	15	$Pnma$	302	61
$(MHy)_2PbBr_4$ (MHy = methylhydrazinium)	4.6 at 348		$Pmn2_1$	349	46
$(4\text{-}CBZACL)_2PbCl_4$ (4-CBZACL = 4-chlorobenzylammonium)	23.3 at 303	55	Orthorhombic ($Cmc2_1$)	496	62
$(BPA)_2PbBr_4$ (BPA = 3-bromopropylammonium)	4.8 at 298	18.2	Orthorhombic ($Cmc2_1$)	375	63
$(PFBA)_2PbBr_4$ ($(PFBA)_2$ = perfluorobenzylammonium)	4.2 at 293	40	Orthorhombic ($Cmc2_1$)	440	64
(Cyclo-Hexanemethylaminium)$_2PbCl_4$	15.4 at 300	1.5	Orthorhombic ($Cmc2_1$)	410	65
(N-Methylcyclohexylammonium)$_2PbCl_4$	2.4 at 340	12	Orthorhombic ($Pmn2_1$)	357	66
Single layer Dion–Jacobson (DJ)					
$(4AMP)PbI_4$	3	3	Orthorhombic ($Pca2_1$)	401	67
$(Mpda)PbBr_4$ (Mpda = N-methyl-1,3-propanediamine divalentcation)	1.7 at 293	0.63	Monoclinic (Pn)	359	68
$(EATMP)PbBr_4$ (EATMP = (2-aminoethyl)trimethyl phosphanium)	0.95 at 358	10	Orthorhombic ($Pma2$)	534	69
Multi-layer RP					
$(C_4H_9NH_3)_2CsPb_2Br_7$	4.2 at 344	6	Orthorhombic ($Cmc2_1$)	412	70
$(BA)_2(EA)_2Pb_3Cl_{10}$ (2; EA = ethylamine)	3 at 290	22	Orthorhombic ($Ama2$)	402	71
$(BA)_3Pb_2Br_7)(EA)_4Pb_3Br_{10}$ (1, EA = ethylamine)	5 at 300	22	Orthorhombic ($Cmc2_1$)	375	72
$(2FEA)(EA)_2Pb_2Cl_{10}$ (2FEA = 2-fluoroethylammonium)	3.5 at 300	19	Orthorhombic ($Cmc2_1$)	411	73
$(IA)_2(EA)_2Pb_3Br_{10}$ (1, IA = isoamylammonium and EA = ethylammonium)	2.2 at 310	2.5	Orthorhombic ($Cmc2_1$)	371	74
$(BA)_2(EA)_2Pb_3I_{10}$	5.09 at 303	5.5	Orthorhombic ($Cmc2_1$)	325	75
(BA = n-butylamine, EA = ethylamine)					
$BA_2MAPb_2Br_7$	3.6 at 318	26	Orthorhombic ($Cmc2_1$)	352	76
$(BA)_2(EA)_2Pb_3Br_{10}$	5 at 300	20	Orthorhombic ($Cmc2_1$)	380	77
$(IBA)_2(EA)_2Pb_3Br_{10}$ (IBA = isobutylammonium)	3.5 at 298	8	Orthorhombic ($Cmc2_1$)	370	78
$(CPA)_2FAPb_2Br_7$ (1, CPA = chloropropylammonium, FA = formamidinium)	5.1 at 300	10	Orthorhombic ($Cmc2_1$)	328	79
$(BA)_2Cs_{0.66}MA_{0.34}Pb_2Br_7$	4.8 at 310	20		379	80
Multi-layered DJ					
$(BDA)(EA)_2Pb_3Br_{10}$ (1, BDA is 1,4-butadiammonium, EA is ethylammonium)	0.47 at 346	7	Orthorhombic ($Ama2$)	363	81

This journal is © The Royal Society of Chemistry 2025

J. Mater. Chem. C, 2025, **13**, 10488–10506 | **10493**

PbX_4^{2-} inorganic octahedral cage can also cause spontaneous polarization. But still, most of the time, the PbX_4^{2-} instability alone is not sufficient to cause polarization unless a motion of the organic cation is coupled with the PbX_4^{2-} octahedral cage. The asymmetry of the coupled separated positive organic cation (MA^+ and BA^+), and negative inorganic metal cation cage (PbX_4^{2-}) in opposite directions creates an internal electric field, which drives spontaneous polarization. Fig. 3(b and c) illustrates the ferroelectric mechanism in an ordered disordered transition of the n-BA (butylammonium) cation coupled with the $MAPbBr_3$ molecules.[97] Fig. 3b shows the cubic structure of the 3D $MAPbBr_3$ HHPs, which transforms into a 2D structure (the right side) after the introduction of the bulky organic BA^+ cations. This coupled BA^+ cation structure leads to possible dynamic reorientation (shown in red arrows), which leads to spontaneous polarization (P_s) in the $(BA)_2MAPb_2Br_7$ structure.

The polarization in the $(BA)_2MAPb_2Br_7$ molecule can originate from the motion: (a) after inserting the BA^+ cation, the $PbBr_6$ octahedra cage is not perfectly symmetric due to strain. Ideally, the bond angles between Br–Pb and Pb–Br are 90°; due to tilting, the bond angle of Br–Pb–Br changes between 87.8° and 92.2°. This structural asymmetry leads to an internal dipole moment between negatively charged (Br^-) and positively charged ions (Pb^{2+}), which creates a spontaneous polarization along the c-axis, as shown (red color arrow) in Fig. 3c. (b) The organic cations (MA^+ and BA^+) are not fixed in the crystal structure ($BA_2MAPb_2Br_7$); they are dynamically reoriented within the structure. The interaction between the reoriented BA^+ and MA^+ undergoes charge separation. Here, order–disorder transitions of positive charge MA^+ cations perfectly align with negative charge Br^- along the c-axis. The resulting dipole moment (yellow color arrow) is shown in Fig. 3c. (c) In the final possible way, hydrogen bonds from the ammonium group

($-NH_3^+$) in the BA^+ organic cation align with the Br^- along the c-axis for the easy dipole moment (N–H···Br) (green color arrow) in Fig. 3c to create spontaneous polarization. Finally, 3D-$MAPbBr_3$ HHPs alone are not sufficient to generate spontaneous polarization. After inserting the BA^+ organic cations into the 3D-$MAPbBr_3$ HHPs, the structure became asymmetric and showed a free dipole orientation, as mentioned above, in three possible ways.

In addition to this, external pressure also strongly affects the HHP's crystal structures; as a result, the HHP material may change its crystal structure from a non-ferroelectric phase to a ferroelectric phase. Juan and others previously studied pressure-dependent polarization in $NH_4Cd(HCOO)_3$ HHPs.[98] Here, the authors vary the pressure from 0 to 18 GPa; at around 10 GPa, the $(NH)_4Cd(HCOO)_3$ material is converted from the orthorhombic ($Pna2_1$) phase to monoclinic (Pc), and both phases are polar non-centrosymmetric phases.[98] Similarly, in 2021, Jung Hoon and their group further confirmed the pressure-induced phase transition on the $MAPbI_3$ HHPs.[99] The authors confirm that $MAPbI_3$ at 0.23 GPa changes its phase from orthorhombic $Fmmm$ to cubic $Im\bar{3}$. This indicates that the inorganic and organic bond lengths and the crystal orientation of $MAPbI_3$ are getting affected at 0.23 GPa. The HHPs' bond length changes are the primary factor that affects the dipole alignment which in turn leads to changes in ferroelectric polarization. In 2024, Szymon and colleagues studied the pressure-dependent ferroelectric transition in 2D-MHy_2PbI_4 HHPs.[100] The study shows that at ambient pressure and room temperature (298 K), MHy_2PbI_4 exists in an orthorhombic ($Pccn$) centrosymmetric crystal structure. When the pressure is increased to 0.07 GPa, the crystal structure changes to orthorhombic ($Pmmn$). Above 1.15 GPa, the crystal structure of MHy_2PbI_4 changes to orthorhombic ($Pmn2_1$), and after 3 GPa,
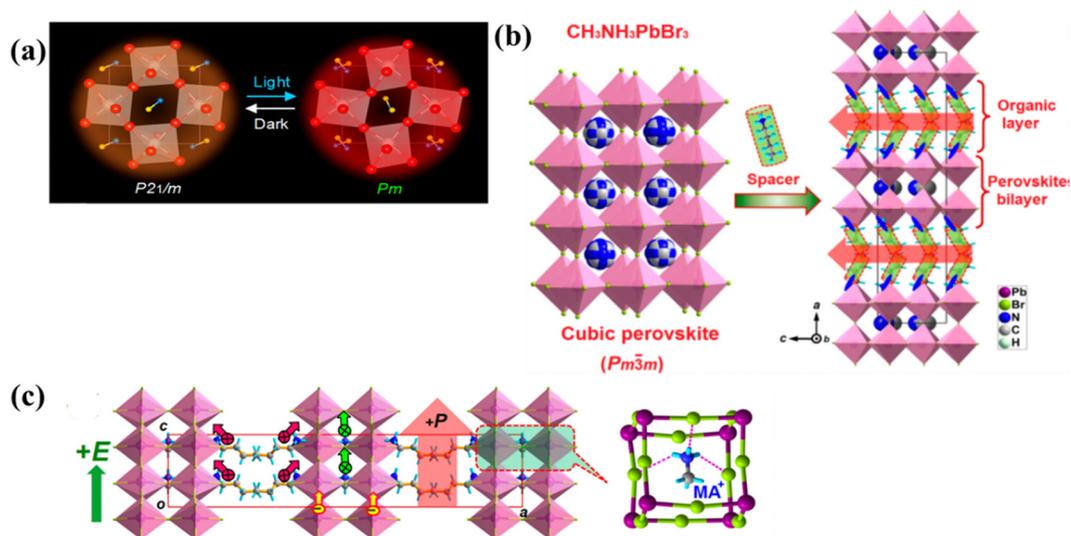

Fig. 3 (a) Light irradiation effect on the crystal structure of the HHP material. Reproduced from ref. 95 with permission from American Chemical Society, copyright 2021. (b) Schematic of cubic perovskite $MAPbBr_3$ and structure modification to $(BA)_2MAPb_2Br_7$ after incorporation of the BA^+ (butylammonium cation) cation and spontaneous polarization in the c-axis, (c) the ferroelectric mechanism in the $(BA)_2MAPb_2Br_7$ HHPs. Reproduced from ref. 97 with permission from American Chemical Society, copyright 2019.

10494 | J. Mater. Chem. C, 2025, 13, 10488–10506

This journal is © The Royal Society of Chemistry 2025

the crystal structure changes to monoclinic ($P2_1$), and both of these are non-centrosymmetric polar phases. Authors further confirmed these structural transformations using X-ray diffraction and second harmonic generation studies. Increasing the pressure alters the PbI_6 octahedral coordination and changes the cation disorder (MHy^+) in the MHy_2PbI_4, leading to changes in its crystal structure. Nonetheless, pressure-induced crystal changes are higher in the HHPs as compared to conventional inorganic and organic materials due to their soft crystal lattice. The pressure effect-dependent ferroelectric polarization leads to pathways for energy-efficient piezoelectric applications and pressure-sensing technologies.

(a) State of the art halide perovskite ferroelectric single crystals

Chen *et al.* in 2019 reported ferroelectric properties in $(ATHP)_2PbBr_4$ (ATHP = 4-aminotetrahydropyran) single crystals with a decent *P–E* hysteresis loop and a $P_s \approx 5.6$ μC cm^{-2} at 363 K as shown in Fig. 4a.[20] The ferroelectric properties of $(ATHP)_2PbBr_4$ are consistently retained up to a high T_C value of 503 K [much higher than that in $BaTiO_3$ (BTO, 393 K)]. And this material has a giant piezoelectric voltage coefficient (g_{33}), which is 660.3×10^{-3} V m N^{-1}, and this value is higher than that of the conventional ferroelectric materials such as $Pb(Zr, Ti)O_3$ (PZT) ceramics ($\sim$20 to 40×10^{-3} V m N^{-1}),[101] and PVDF (286.7×10^{-3} V m N^{-1}).[102] The g_{33} is a piezoelectric voltage coefficient that describes the electrical voltage generated under mechanical stress in the same direction as the applied voltage. Fig. 4b shows the temperature dependence of the dielectric constant (ε') during heating and cooling cycles of $(ATHP)_2PbBr_4$. A material phase transition around 510 K is observed, which is a hallmark of ferroelectric behaviour. The authors claimed that the $(ATHP)_2PbBr_4$ material has the highest g_{33} and T_C among all existing HHPs reported up to 2019. The $(ATHP)_2PbBr_4$ single

crystal displays superior ferroelectric properties caused by its particular structural and chemical composition. Fig. 4c shows the *ab* plane arrangement of the C, H, O, N, Pb, and Br atoms of a 2D layered single crystal $(ATHP)_2PBr_4$ perovskite. The atoms' distribution confirms the layered nature of the perovskite, which is key to its extraordinary ferroelectric properties. Fig. 4d shows a side view of the crystal structure along the *bc*-plane, revealing also the atom connectivity and organization in this plane, underlining continuity between layers. Finally, Fig. 4e depicts another cartoon of the 2D crystal structure in the *ac*-plane of the single crystal $(ATHP)_2PbBr_4$ perovskite. This describes in even more detail the bonding and spatial structure, which is critical for understanding these materials' ferroelectricity and piezoelectric properties. From Fig. 4c, it is observed that the organic ATHP cations interact with the inorganic $PbBr_4$ layers through hydrogen bonding. The hydrogen bonding connectivity, along with structural factors such as cation tilting and rotation coupled with inorganic layers of HHPs, plays a crucial role in stabilizing the non-centrosymmetric phases. However, this condition alone is not sufficient for spontaneous polarization, and dipole alignment is also important; otherwise, both dipoles cancel each other out. For example, in $(MHy)_2PbBr_4$ HHPs at 380 K, even though it has strong hydrogen bonding with organic cations and inorganic layers, anti-parallel dipole arrangement leads to net zero spontaneous polarization in this molecule.[46] The carbon atoms in ATHP organic molecules help the structural rigidity and influence the orientation of the organic cations within the lattice. The polarization value (5.6 μC cm^{-2}) of $ATHP_2PbBr_4$ HHPs is relatively higher than most of the HHP perovskites mentioned in Table 1. This is probably due to the significant displacement of Pb atoms and the unique structural alignment of the ATHP cations. The large organic cations in ATHP might
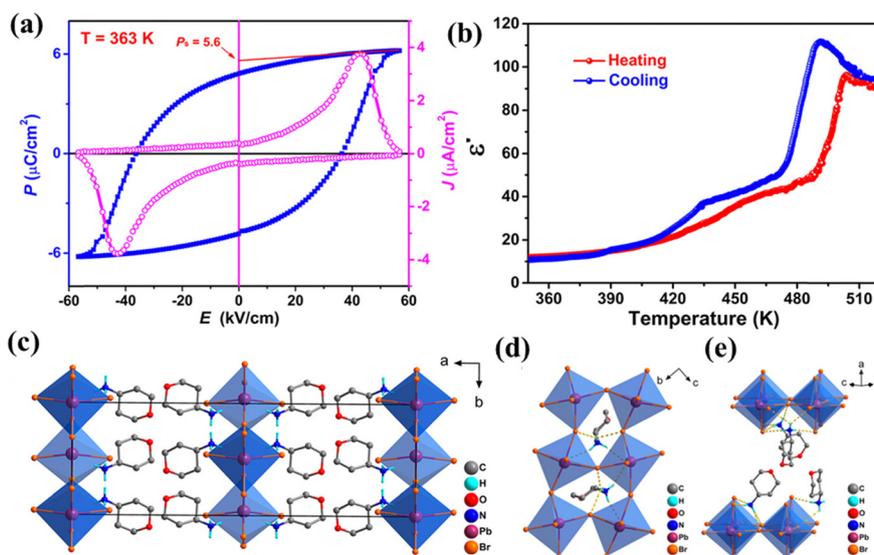

Fig. 4 (a) Polarization−electric field (*P–E*) hysteresis loop of single crystal $(ATHP)_2PbBr_4$ perovskites at 363 K. (b) Graph showing the temperature dependence of the $(ATHP)_2PbBr_4$ perovskite dielectric constant (ε') during heating and cooling cycles. (c) $(ATHP)_2PbBr_4$ layered perovskite along the *ab*-plane, (d) $(ATHP)_2PbBr_4$ layered perovskite along the *bc*-plane, and (e) $(ATHP)_2PbBr_4$ layered perovskite along the *ac*-plane. Reproduced from ref. 20 with permission from the American Chemical Society, copyright 2020.
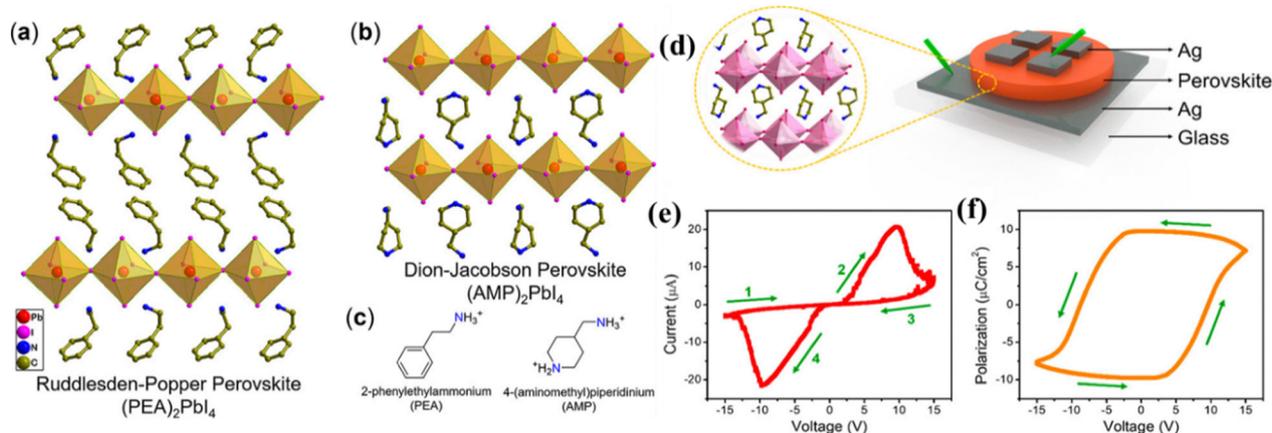
This journal is © The Royal Society of Chemistry 2025

J. Mater. Chem. C, 2025, **13**, 10488–10506 | **10495**

Fig. 5 (a) The crystal structure of the Ruddlesden–Popper perovskite, $(PEA)_2PbI_4$, (b) Dion–Jacobson perovskite $(4AMP)PbI_4$ crystal structure, (c) chemical structure of the organic cations, (d) single crystal ferroelectric sample structure, (e) current–voltage (I–V) hysteresis plot, and (f) polarization–voltage (P–V) hysteresis loop. Reproduced from ref. 104 with permission from American Chemical Society, copyright 2019.

create larger dipole moments, contributing to the higher overall polarization.

The crystal structure of typical 2D layered Ruddlesden–Popper $(PEA)_2PbI_4$ perovskites consisting of lead iodide PbI_6 octahedra separated by organic double corner-shared 2-phenylethylammonium (PEA) organic cations is shown in Fig. 5a. Fig. 5b shows the crystal structure of Dion–Jacobson perovskite $(4AMP)PbI_4$ consisting of lead iodide (PbI_6) octahedra layers with 4-(aminomethyl) piperidinium (4AMP) cations intercalated between them. The distinct layering in the Dion–Jacobson perovskite $(4AMP)PbI_4$ is due to the shorter interlayer bifunctional nature of the $4AMP^{2+}$ cations to form stronger hydrogen bonds between the inorganic (PbI_6) layers. This leads to stable interlayer coupling as compared to $(PEA)_2PbI_4$ HHPs. In the $(PEA)_2PbI_4$ HHPs, a weaker van der Waals force will connect the PbI_6 layers, and the interlayer distance is longer than in $(4AMP)PbI_4$. Fig. 5c illustrates the chemical structures of the organic cations employed in Ruddlesden–Popper (2-phenylethylammonium, PEA) and Dion–Jacobson perovskites [4-(aminomethyl)piperidinium, AMP]. The sample structure for measurements of ferroelectric properties in a $(4AMP)PbI_4$ single crystal is shown schematically in Fig. 5d. The current switching hysteresis loop of the $(4AMP)PbI_4$ single crystal in Fig. 5e implies the material to be ferroelectric, and numbering from 1 to 4 indicates different current switching states achieved during its switching process. Fig. 5f shows the hysteresis of the polarization–voltage (P–V), showing remanent polarization (10 μC cm^{-2}) and coercive field. The $(4AMP)PbI_4$ Dion–Jacobson perovskites exhibit the Rashba effect, which involves spin-band splitting caused by the absence of inversion symmetry and spin–orbit coupling in a material. Such a Rashba effect can enhance the charge carrier separation and mobility, making it beneficial to stabilize polar phases, thereby improving the ferroelectric properties of the material.[103]

In 2025, Yu Ma and group reported the first study on the ferroelectric behavior in the single crystal HHP heterostructure $(EA_3Pb_2Br_7)(EA)_4Pb_3Br_{10}$ ($n = 2/3$).[105] Here, the authors used

neopentylamine (NPA), a molecular scissor, as a self-assembling layer to develop the $(EA_3Pb_2Br_7)(EA)_4Pb_3Br_{10}$ structure. In the $n = 2/3$ heterostructure, the bulkier size of the neopentyl ($-C(CH_3)_3$) group increases the structural asymmetry, which leads to enhanced polarization. Here, ethylamine (EA) acts as a spacer between the $n = 2/3$ heterostructure; due to its smaller size, it stabilizes the hydrogen bonding network and stacks the layer periodic layer thickness as shown in Fig. 6a. The ferroelectric polarization value of the ($n = 2/3$) heterostructure is higher than the individual $n = 2$ & 3 as shown in the P–E hysteresis loop in Fig. 6b. The saturation polarizations of $n = 2$, 3 & $n = 2/3$ are 3.1, 4 & 5 μC cm^{-2} respectively. The enhanced polarization in the heterostructure is due to an increased fourfold reorientation disorder of EA organic cations, allowing higher net dipole moments. In addition to this, temperature-dependent P–E hysteresis loops of the $n = 2/3$ heterostructure from 300 to 320 K confirm that this material has strong polarization retention in this range as shown in Fig. 6c. This material further confirms that in the ferroelectric fatigue test, heterostructure ($n = 2/3$) maintained its stable polarization states for up to 120 000 cycles, as shown in Fig. 6d. However, in the case of $n = 2$ & 3 individuals, their polarization states are not stable for more than around 50 000 cycles; this confirms that the heterostructure has excellent fatigue resistance.

Table 1 shows that most of the 2D HHP ferroelectrics are in the orthorhombic ($Cmc2_1$) crystal structure. This crystal structure is the most energetically favorable and thermodynamically stable structure compared to other ferroelectric phases (monoclinic or tetragonal phases).[106] Most of the 2D HHP ferroelectrics listed in Table 1 are RP phase. The RP phase is more stable than DJ due to its larger interlayer spacing and flexibility. At the same time, ferroelectric polarization is also relatively larger in the RP phase than in DJ. In 2024, Wang N. & group showed the highest ferroelectric polarization (23.3 μC cm^{-2}) in $(4-CBZACL)_2PbCl_4$ 2D single layer RP HHPs. The authors claim that the *para*-chlorine substitution in the $(4-CBZACL)_2PbCl_4$ molecule enhances the dipole alignment and octahedral
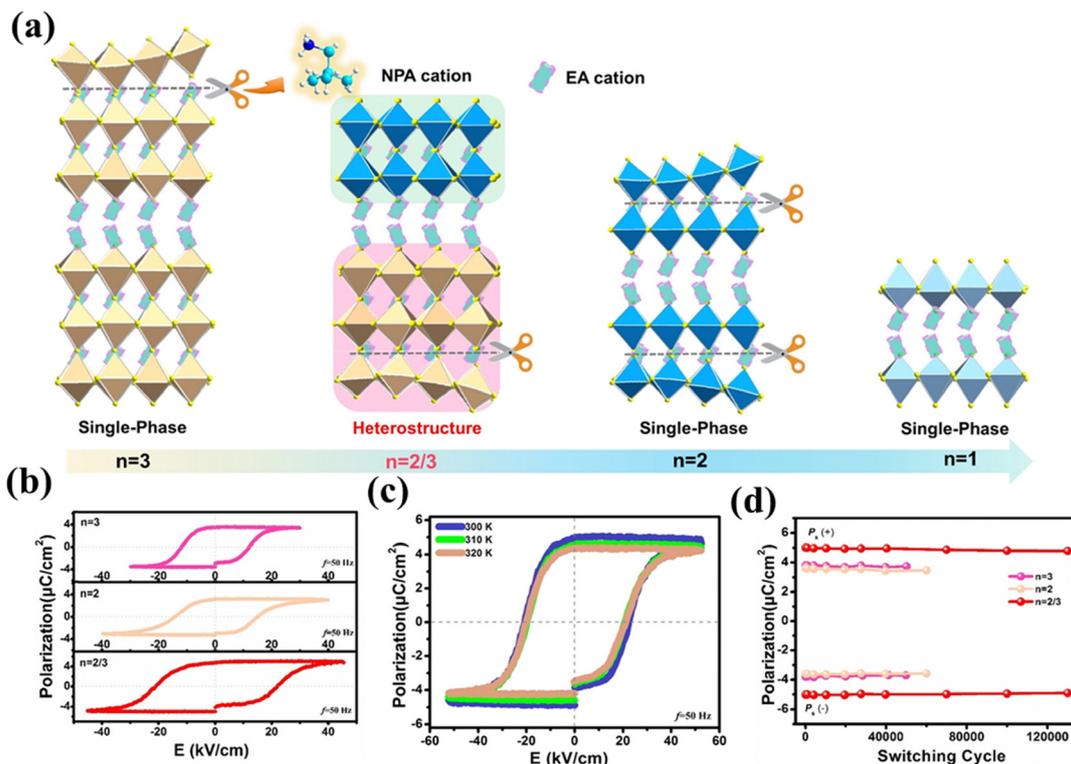
10496 | *J. Mater. Chem. C*, 2025, **13**, 10488–10506

This journal is © The Royal Society of Chemistry 2025

Fig. 6 (a) The figure illustrates self-assembling heterostructure $(EA)_2(EA)_{n-1}Pb_nBr_{3n+1}$ (n = 2/3) and individuals n = 1 to 3 single crystal halide hybrid perovskites, (b) ferroelectric P–E hysteresis loops at 50 Hz, (c) the P–E loops of n = 2/3 heterostructures at different temperatures, and (d) the fatigue test for n = 2, n = 2/3, n = 3. Reproduced from ref. 72 with permission from John Wiley and Sons, copyright 2025.

distortion, leading to enhanced polarization.[62] The coercive field in the 2D-RP HHPs ranges from around 2 to 500 kV cm^{-1}, which is relatively larger than the multi-layered (quasi-2D) RP phase. The 2D RP single layer has strong dielectric confinement compared to the multi-layered structure, resulting in a higher energy to switch the polarization state.[107]

(b) Ferroelectric HHP thin films

Zhang *et al.* have shown the ferroelectric properties of $(PEA)_2(MA)_{n-1}Pb_nI_{3n+1}$ thin films with n varying from 2 to ∞. Fig. 7a shows a schematic Ag/PCBM/$(PEA)_2(MA)_{n-1}Pb_nI_{3n+1}$/PEDOT:PSS/ITO-Glass of the layer structure of a perovskite-based device used in the study of ferroelectric behavior. Fig. 7b shows the P–E loop of the $(PEA)_2(MA)_{n-1}Pb_nI_{3n+1}$ (n = 5) perovskite thin film. The polarization is not saturated even at higher electric fields, and the loop is somewhat open, indicating incomplete polarization switching. However, the observed unsaturated P–E loop shows a resistive behavior at a higher electric field likely because of the dominant ion migration over ferroelectricity, indicated by the circle-shaped loop. Thinner layers of perovskite ~300 nm might not exhibit saturated polarization due to the insufficient material volume to support full domain switching. The coercive field is reducing $(PEA)_2(MA)_{n-1}Pb_nI_{3n+1}$ from n = 2 to 5, as shown in Fig. 7c; this may be due to reduced dimensional confinement compared to lower n values, making it easier for domain walls to move, reducing the energy barrier

for polarization switching and thus lowering the coercive field. As shown in Fig. 7d, the polarization increases with the n value, which is typically due to better dipole alignment and less disruption from organic cations, which results in higher net polarization for organic spacers at n = 5. The n = 5 (quasi 2D) structure represents an optimal balance between 2D and 3D characteristics, resulting from higher P_s and lower E_C.

Fig. 7e and f show the PFM image recorded for thin film $(PEA)_2(MA)_{n-1}Pb_nI_{3n+1}$ (n = 5) ferroelectric at -4 V poling voltage and the corresponding dipole orientation in the upward direction. Switching this poling voltage to +4 V, the dipole orientation direction is reversed, and the corresponding phase plot can be seen in images Fig. 7g and h respectively. The dipole switching with the field confirms the ferroelectric features in $(PEA)_2(MA)_{n-1}Pb_nI_{3n+1}$ (n = 5). Fig. 7i and j show the PFM amplitude and PFM phase plots of $(PEA)_2(MA)_{n-1}Pb_nI_{3n+1}$ perovskite thin films (n = 2 to n = ∞). As n increases from 2 to 5, the width of the PFM hysteresis amplitude loops increases, and this affects the remnant polarization. MAPbI$_3$ (n = ∞) shows the lower coercive field with narrow phase width suggesting minimal ferroelectric behavior compared to other compositions, which is due to the lack of layered structure in 3D. Among all, n = 5 shows wider amplitude PFM hysteresis loops, indicating less polarization retention, and at the same time, the PFM phase plots become wider, indicating increased polarization stability. For the same thin film $(PEA)_2(MA)_{n-1}Pb_nI_{3n+1}$ (n = 2 to n = ∞) perovskite material though the P–E loop is
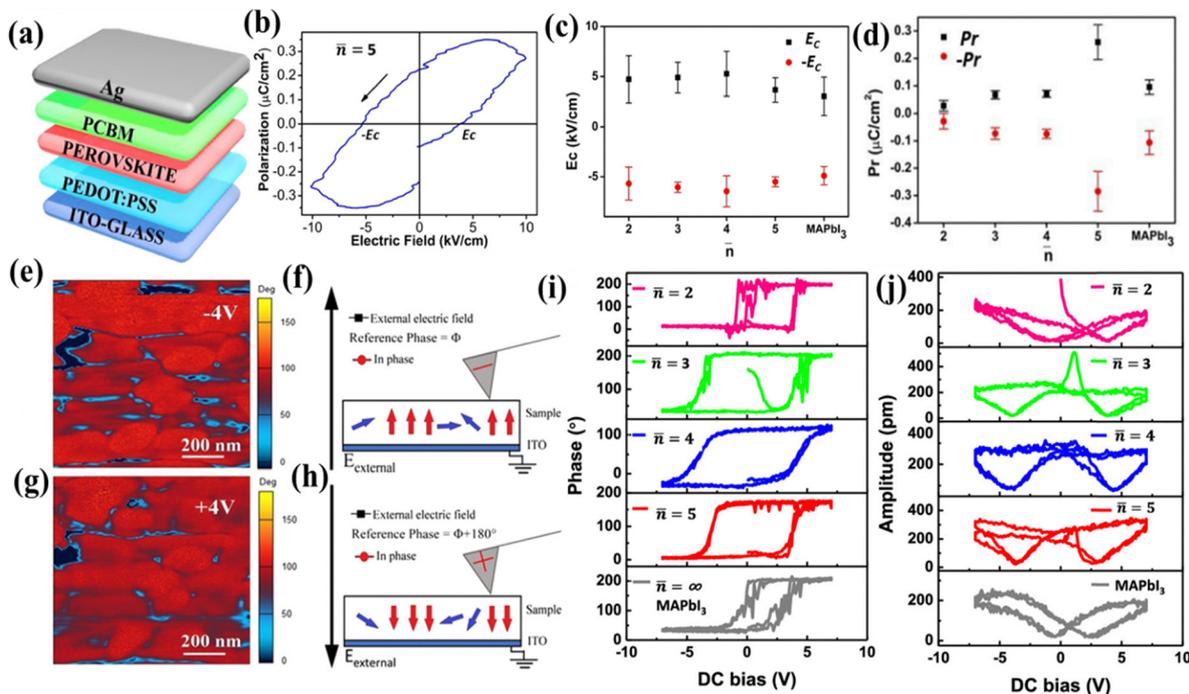
This journal is © The Royal Society of Chemistry 2025

J. Mater. Chem. C, 2025, **13**, 10488–10506 | **10497**

Fig. 7 (a) Ferroelectric device structure of the $(PEA)_2(MA)_{n-1}Pb_nI_{3n+1}$ perovskite, (b) polarization−electric field (P−E) loop, (c) coercive field (E_c) plot of $(PEA)_2(MA)_{n-1}Pb_nI_{3n+1}$ with n = 2 to ∞, (d) polarization (P_s) plot of $(PEA)_2(MA)_{n-1}Pb_nI_{3n+1}$ with n = 2 to ∞, piezoresponse force microscopy, (e) and (g) micrograph at −4 V & +4 V poling (n = 5), (f) and (h) dipoles switching plots at −4 V & +4 V (n = 5), (i) hysteresis phase plot of n = 2 to ∞, (j) amplitude plot of n = 2 to ∞.[108] Reproduced from ref. 108 with permission from American Chemical Society, copyright 2019.

measured by using the Sawyer–Tower circuit technique, no indication of ferroelectric behavior could be observed. The Sawyer–Tower circuit measures macroscopic polarization, which might not capture subtle or nanoscale ferroelectric features present in $(PEA)_2(MA)_{n-1}Pb_nI_{3n+1}$ (n = 2 to n = ∞) perovskite thin films. PFM is more sensitive to local piezoresponse and can detect ferroelectric domains in $(PEA)_2(MA)_{n-1}Pb_nI_{3n+1}$ (n = 2 to n = ∞) at the nanoscale, revealing ferroelectric properties which were not observed in bulk measurements.[109]

In 2023, B. Han *et al.* are the first to show the saturated P–E loops with proper current switching of the $(3\text{-PyA})_2PbI_4$ (PyA-pyridinium acetate iodide) (2D), $(FA)_{0.7}Cs_{0.3}PbI_{2.08}Br_{0.92}$ (3D) and 2D/3D thin film HHPs using the double wave ferroelectric tester.[110] Fig. 8a–c show the I–P–E graphs of the PEN/ITO/SAM/(2D),

(3D), and (2D/3D)/PCBM/BCP/Ag device structure, respectively. The $(3\text{-PyA})_2PbI_4$ (2D) HHPs show higher saturation polarization (12.78 µC cm^{-2}) as compared to the stacked 2D over $(FA)_{0.7}Cs_{0.3}PbI_{2.08}Br_{0.92}$ perovskites shown in Fig. 8a. Generally, 2D perovskites have confined charge carriers in their layered structure; this confinement leads to a strong interaction between the organic and inorganic molecules, which leads to higher spontaneous polarization. Another reason is the confined organic cation, which creates a strong dipolar interaction with displaced hydrogen bondings in the crystal structures. In the case of $(FA)_{0.7}Cs_{0.3}PbI_{2.08}Br_{0.92}$ (3D) perovskites, the P–E loops and respective current look like resistive as shown in Fig. 8b. It is clear that $(FA)_{0.7}Cs_{0.3}PbI_{2.08}Br_{0.92}$ thin films do not show any ferroelectric nature; this is probably due to this molecule having a symmetric isotropic crystal structure with a
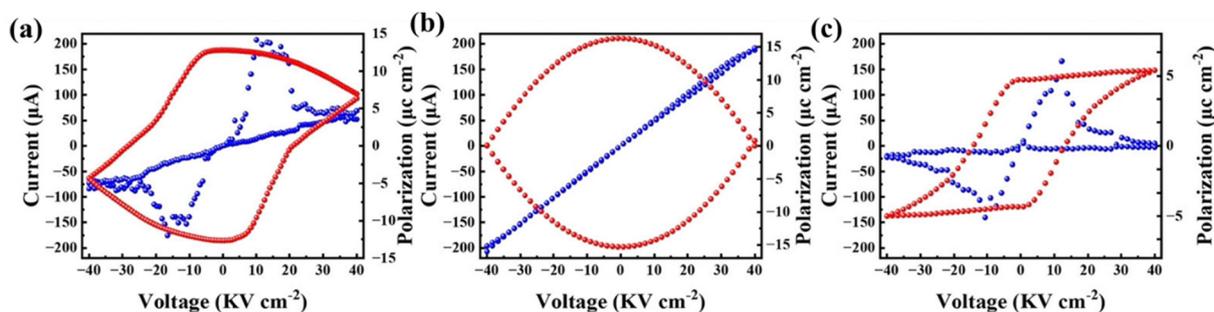

Fig. 8 Polarization−electric (P−E) field hysteresis ferroelectric loop of (a) $(3\text{-PyA})_2PbI_4$ (2D), (b) $(FA)_{0.7}Cs_{0.3}PbI_{2.08}Br_{0.92}$ (3D), and (c) $(3\text{-PyA})_2PbI_4$/$(FA)_{0.7}Cs_{0.3}PbI_{2.08}Br_{0.92}$ halide perovskite thin films. Reproduced from ref. 110 with permission from John Wiley and Sons, copyright 2021.

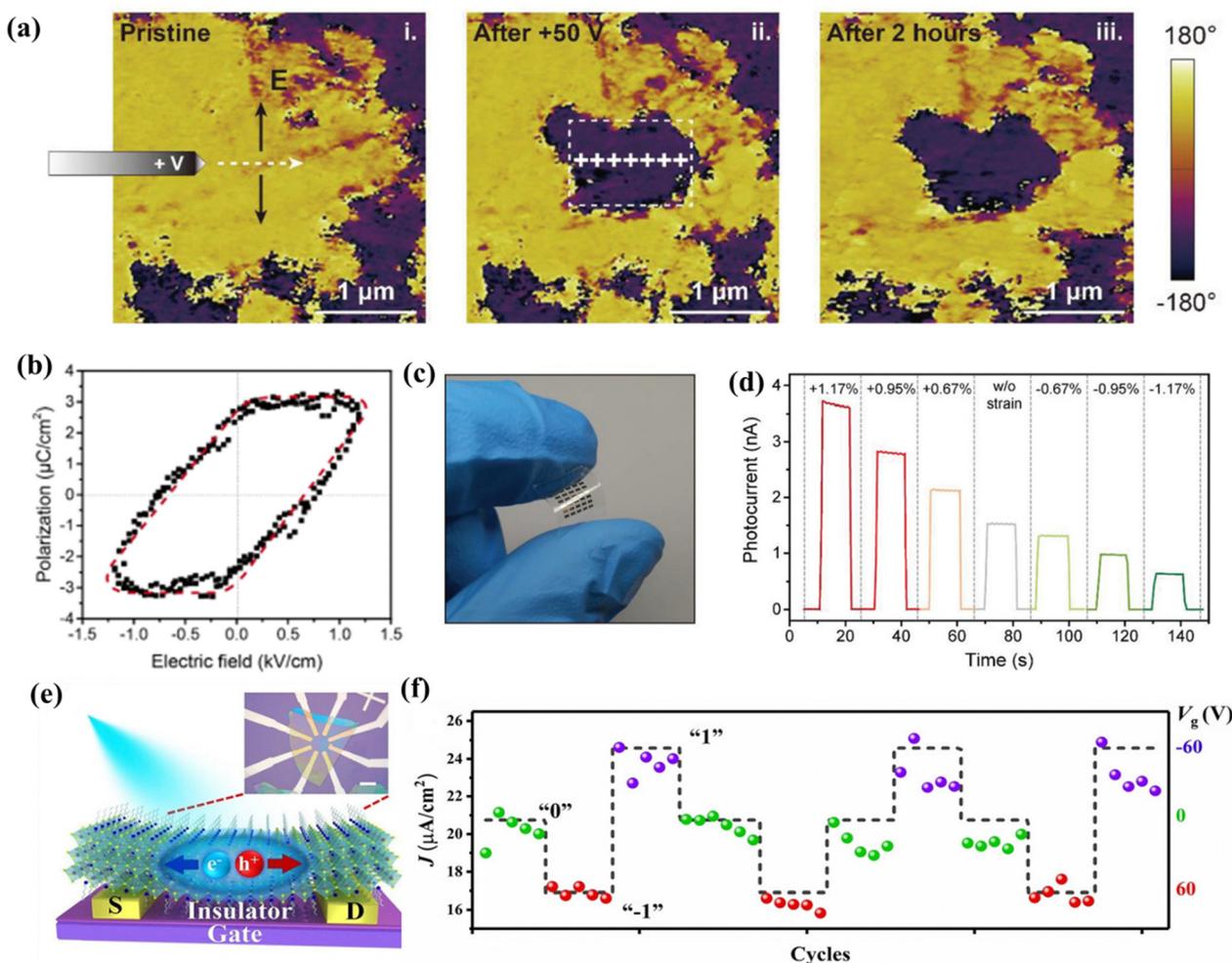10498 | *J. Mater. Chem. C*, 2025, **13**, 10488–10506

This journal is © The Royal Society of Chemistry 2025

Fig. 9 (a) Thin film HHPs $(EA)_4Pb_3Br_{10}$ piezoresponse force microscopy (PFM) phase image during polarization switching, (i) phase image before applying the +50 V to the PFM tip, (ii) phase domains are switched because of +50 V tip bias, (iii) the ferroelectric domains up to 2 h, (b) P–E loops of the $(EA)_4Pb_3Br_{10}$ SCFs at a frequency of 3.33 kHz, (c) schematic of flexible $(EA)_4Pb_3Br_{10}$ HHPs, (d) photo switching characteristics of thin film HHPs $(EA)_4Pb_3Br_{10}$ under different strain. Reproduced from ref. 112 with permission from John Wiley and Sons, copyright 2021. (e) The schematic of $(HA)_2MA_2Pb_3Br_{10}$ HHPs' ferroelectric field effect transistor memory, (f) the ferroelectric device memory working mechanism with a pulse (with reading and writing bit 1 & 0). Reproduced from ref. 113 with permission from John Wiley and Sons, copyright 2023.

less confined structure as compared to the 2D perovskite. The authors further verified the non-ferroelectric & ferroelectric properties of $(FA)_{0.7}Cs_{0.3}PbI_{2.08}Br_{0.92}$, and $(3\text{-PyA})_2PbI_4$ molecules with the DFT simulations. Here they found that the $(3\text{-PyA})_2PbI_4$ molecule has an asymmetric crystal structure, which leads to a strong dipole moment. In the hybrid 2D/3D perovskite structure, the saturation polarization is 5.1 μC cm^{-2}. Here, by inserting the $(3\text{-PyA})_2PbI_4$ molecule over the $(FA)_{0.7}Cs_{0.3}PbI_{2.08}Br_{0.92}$ perovskite, one can somewhat interrupt the collective dipole moment in the $(3\text{-PyA})_2PbI_4$ perovskite, which leads to lower polarization values as compared to the 2D structure.

Thin film $(EA)_4Pb_3Br_{10}$ HHPs' PFM phase image in Fig. 9a(i) confirms the random distribution of dark and bright regions, which suggests that ferroelectric domains are unswitched. After applying the +50 V PFM tip bias, the image in Fig. 9a(ii) shows new switched domains with opposite phase contrast. This confirms that $(EA)_4Pb_3Br_{10}$ HHPs have switchable ferroelectric domains under external fields. After 2 hours, the ferroelectric domains are clear and stable, as shown in Fig. 9a(iii); this confirms that the material has a good polarization retention over time. Thin film $(EA)_4Pb_3Br_{10}$ HHPs' P–E loop at 3.33 kHz is measured using the Sawyer–Tower circuit shown in Fig. 9b. These ferroelectric P–E loops confirm that $(EA)_4Pb_3Br_{10}$ HHPs are not well saturated, and it looks like this material shows high leakage behavior when measured over a large area. However, this could be because the thin films of HHPs are typically polycrystalline, known to have higher defect density and grain boundaries as compared to single crystals. This is due to the crystallization process of thin films in which there would be several individual grains nucleating and growing independently till they meet each other. These resultant grains and boundaries increase the leakage current, which ultimately degrades the ferroelectric properties in thin films of HHPs. Among all the low-dimensional HHP polycrystalline thin films,

This journal is © The Royal Society of Chemistry 2025

J. Mater. Chem. C, 2025, 13, 10488–10506 | 10499

ion migration is significantly increased at grain boundaries because of their specific structural and chemical features.[111] However, this migration of ions can create local electric fields, counter to the applied field, which in turn reduces net polarization. Grain boundaries generally contain more defects, vacancies, and dislocations than grain interiors. These defects provide pathways with lower activation energies for ion movement, making it easier for ions to migrate along grain boundaries than through the bulk of the grains.[111] With the large concentration of defects, grain boundaries can inhibit the polarization domains from connecting in a straight line, reducing the overall polarization efficiency. These grain boundary effects are more significant in large areas of ferroelectrics. The $(EA)_4Pb_3Br_{10}$ HHP thin film ferroelectric effect is confirmed by PFM, but not with the Sawyer–Tower P–E loop measurement. The PFM scanned $(EA)_4Pb_3Br_{10}$ ferroelectric device active area is less than the Sawyer–Tower ferroelectric tester measured active area. Recently, our group (Muddam *et al.*) also studied the ferroelectric response in thin film $BA_2MA_{n-1}Pb_nBr_{3n+1}$ ($n = 1$ & 2) HHPs using the PFM and Sawyer–Tower circuit method.[28] Here, we understand that macroscopic polarization values from a large ferroelectric device area (0.1 cm^2), confirmed by the Sawyer–Tower P–E loop, have a higher leakage current as compared to a small area (210 μm × 30 μm) ferroelectric response from the PFM method. In addition to this, ion migration also contributes to the instability in the ferroelectric hysteresis P–E loops that leads to poor performance in applications such as memory devices and energy harvesting systems. Meanwhile, the single crystals of HHPs have a coherent crystal structure with no interruption. Since single crystals lack grain boundaries, the issues associated with these boundaries, such as increased ion migration and defect-related charge carrier pathways, are absent. Single crystals have a uniform structure, which reduces the phonon scattering and ion migration, which enhances their ferroelectric properties. In addition to this, $(EA)_4Pb_3Br_{10}$ HHPs are prepared on a flexible plastic substrate for the piezo photonic response as shown in Fig. 9c. Each pulse peak shown in Fig. 9d corresponds to an on–off cycle of light exposure. The pulses show different strain values (+1.17%, +0.95%, 0%, −0.67%, and −1.17%); all the pulses show fast and reversible photo switching. Under tensile strain (+%), the photocurrent increases compared to compressive strain (−%), confirming that +% tensile strain improves charge carrier transport. Without any strain, photo-charge carriers' performance is higher than the compressive strain, which indicates that the charge carriers' flow is hindered under compressive strain. The strain-dependent piezo photonic response of HHPs holds significant potential for application in wearable optoelectronic devices. In 2023, Haojie & group fabricated $(HA)_2MA_2Pb_3Br_{10}$ (HA = hexylammonium) HHP thin films for ferroelectric field effect transistor memory, as shown in Fig. 9e. It is a simple three-terminal device (source, drain, and gate). Here, the gate bias control is used to determine the direction of the ferroelectric domain alignment, which sets the FERAM state for reading or writing binary bits, either 1 and 0, as shown in Fig. 9f. Initially, the ferroelectric FET device state is zero under zero gate voltage ($V_g = 0$); this memory state corresponds to the reading condition. Under a negative switching pulse ($V_g = −60$ V), all the ferroelectric dipoles will switch to a specific direction, and this state is considered a stable polarization state as ($P−$) and the corresponding storing binary bit is zero. Similarly, under positive gate voltage ($V_g = +60$ V), all the ferroelectric dipoles switch to the opposite direction of the negative gate supply, which leads to a positive polarization state ($P+$). And this state corresponds to storing binary bit 1. The HHP FERAMs are essential in the generation of data storage due to their simple, low-cost solution processing and easy integration with flexible & wearable electronics. Their multi-functional (piezoelectric, ferroelectric, and light absorbance) properties make HHPs a single device for self-powered, high-density modern computing and data storage applications.

4. Conclusion

This review systematically examined the ferroelectric properties of various halide perovskites with emphasis on layered 2D single crystal and thin film HHP materials. Compared to 3D HHPs, 2D perovskites show enhanced saturated polarisation, higher Curie temperature and higher coercive field in general. Our comprehensive review shows that while in the case of halide perovskite single crystals, the most commonly used technique to confirm the ferroelectric properties is the Sawyer–Tower method (macroscopic), this method can be challenging in thin film halide perovskites especially when additional layers are included. However successful application of this technique to thin films is also emerging. As of now, PFM (microscopic) is the most commonly used technique to characterize ferroelectricity in halide perovskite thin films. This may be because thin film HHPs have surface defects that influence the bulk performance of thin films, thereby quenching their ferroelectric properties and making it very difficult to detect using macroscopic ferroelectric techniques. This review gives the current status and challenges of ferroelectric properties in thin film HHPs. We suggest that it is more important to passivate the surface and interface defects in the HHP thin films to achieve better ferroelectric properties, especially for future ferroelectric applications like FeRAM in neuromorphic computing and self-charging flexible electronics applications.

Data availability

No primary research results, software or code have been included, and no new data were generated or analysed as part of this review.

Conflicts of interest

There are no conflicts to declare.

10500 | *J. Mater. Chem. C*, 2025, **13**, 10488–10506

This journal is © The Royal Society of Chemistry 2025

Acknowledgements

References

1 M. Manzi, G. Pica, M. De Bastiani, S. Kundu, G. Grancini and M. I. Saidaminov, Ferroelectricity in Hybrid Perovskites, NLM (Medline), *J. Phys. Chem. Lett.*, 2023, **14**(14), 3535–3552.

2 S. Shahrokhi, W. Gao, Y. Wang, P. R. Anandan, M. Z. Rahaman, S. Singh, D. Wang, C. Cazorla, G. Yuan, J. M. Liu and T. Wu, Emergence of Ferroelectricity in Halide Perovskites, *Small Methods*, 2020, **4**(8), 2000149, DOI: 10.1002/SMTD.202000149.

3 R. Ding, Y. Lyu, Z. Wu, F. Guo, W. F. Io, S. Pang, Y. Zhao, J. Mao, M. Wong and J. Hao, Effective Piezo-Phototronic Enhancement of Flexible Photodetectors Based on 2D Hybrid Perovskite Ferroelectric Single-Crystalline Thin-Films, *Adv. Mater.*, 2021, **33**(32), 2101263, DOI: 10.1002/adma.202101263.

4 Z. Guo, J. Li, R. Chen and T. He, Advances in single crystals and thin films of chiral hybrid metal halides, *Prog. Quantum Electron.*, 2022, **82**, 100375.

5 S. Ippili, V. Jella, A. M. Thomas and S.-G. Yoon, The Recent Progress on Halide Perovskite-Based Self-Powered Sensors Enabled by Piezoelectric and Triboelectric Effects, *Nanoenergy Adv.*, 2021, **1**, 3–31.

6 N. Meng, X. Ren, X. Zhu, J. Wu, B. Yang, F. Gao, H. Zhang, Y. Liao, E. Bilotti, M. J. Reece and H. Yan, Multiscale understanding of electric polarization in poly(vinylidene fluoride)-based ferroelectric polymers, *J. Mater. Chem. C*, 2020, **8**, 16436–16442.

7 N. Izyumskaya, Ya Alivov and H. Morkoç, Oxides, Oxides, and More Oxides: High-κ Oxides, Ferroelectrics, Ferromagnetics, and Multiferroics, *Crit. Rev. Solid State Mater. Sci.*, 2009, **34**, 89–179.

8 V. Pecunia, S. R. P. Silva, J. D. Phillips, E. Artegiani, A. Romeo, H. Shim, J. Park, J. H. Kim, J. S. Yun, G. C. Welch, B. W. Larson, M. Creran, A. Laventure, K. Sasitharan, N. Flores-Diaz, M. Freitag, J. Xu, T. M. Brown, B. Li, Y. Wang, Z. Li, B. Hou, B. H. Hamadani, E. Defay, V. Kovacova, S. Glinsek, S. Kar-Narayan, Y. Bai, D. Bin Kim, Y. S. Cho, A. Žukauskaitė, S. Barth, F. R. Fan, W. Wu, P. Costa, J. del Campo, S. Lanceros-Mendez, H. Khanbareh, Z. L. Wang, X. Pu, C. Pan, R. Zhang, J. Xu, X. Zhao, Y. Zhou, G. Chen, T. Tat, I. W. Ock, J. Chen, S. A. Graham, J. S. Yu, L.-Z. Huang, D.-D. Li, M.-G. Ma, J. Luo, F. Jiang, P. S. Lee, B. Dudem, V. Vivekananthan, M. G. Kanatzidis, H. Xie, X.-L. Shi, Z.-G. Chen, A. Riss, M. Parzer, F. Garmroudi, E. Bauer, D. Zavanelli, M. K. Brod, M. Al Malki, G. J. Snyder, K. Kovnir, S. M. Kauzlarich, C. Uher, J. Lan, Y.-H. Lin, L. Fonseca, A. Morata, M. Martin-Gonzalez, G. Pennelli, D. Berthebaud, T. Mori, R. J. Quinn, J.-W. G. Bos, C. Candolfi, P. Gougeon, P. Gall, B. Lenoir, D. Venkateshvaran, B. Kaestner, Y. Zhao, G. Zhang, Y. Nonoguchi, B. C. Schroeder, E. Bilotti, A. K. Menon, J. J. Urban, O. Fenwick, C. Asker, A. A. Talin, T. D. Anthopoulos, T. Losi, F. Viola, M. Caironi, D. G. Georgiadou, L. Ding, L.-M. Peng, Z. Wang, M.-D. Wei, R. Negra, M. C. Lemme, M. Wagih, S. Beeby, T. Ibn-Mohammed, K. B. Mustapha and A. P. Joshi, Roadmap on energy harvesting materials, *J. Phys. Mater.*, 2023, **6**, 042501.

9 E. Fabbri, X. Cheng, T. J. Schmidt, J. Casanova-Chafer, R. Garcia-Aboal, P. Atienzar, A. Al Mamun, Y. Mohammed, P. Nandi, D. Topwal, N.-G. Park and H. Shin, Organic-inorganic hybrid lead halides as absorbers in perovskite solar cells: a debate on ferroelectricity, *J. Phys. D: Appl. Phys.*, 2020, **53**, 493002.

10 R. Pandey, G. Vats, J. Yun, C. R. Bowen, A. W. Y. Ho-Baillie, J. Seidel, K. T. Butler and S. Il Seok, Mutual Insight on Ferroelectrics and Hybrid Halide Perovskites: A Platform for Future Multifunctional Energy Conversion, *Adv. Mater.*, 2019, **31**, 1807376.

11 Q. Chen, N. De Marco, Y. Yang, T. Bin Song, C. C. Chen, H. Zhao, Z. Hong, H. Zhou and Y. Yang, Under the spotlight: The organic–inorganic hybrid halide perovskite for optoelectronic applications, *Nano Today*, 2015, **10**, 355–396.

12 Y. Gui, J. Shen, Y. Zhou, R. Wang, Y. Yang and J. Xue, Inorganic surface passivation strategies of metal halide perovskites, *Inf. Funct. Mater.*, 2024, **1**, 207–219.

13 M. Lun, C. Su, J. Li, Q. Jia, H. Lu, D. Fu, Y. Zhang and Z. Zhang, Introducing Ferroelasticity into 1D Hybrid Lead Halide Semiconductor by Halogen Substitution Strategy, *Small*, 2023, **19**(49), e2303127, DOI: 10.1002/smll.202303127.

14 H.-Y. Zhang, Z.-X. Zhang, X.-G. Chen, X.-J. Song, Y. Zhang and R.-G. Xiong, Large Electrostrictive Coefficient in a Two-Dimensional Hybrid Perovskite Ferroelectric, *J. Am. Chem. Soc.*, 2021, **143**, 1664–1672.

15 X.-G. Chen, X.-J. Song, Z.-X. Zhang, H.-Y. Zhang, Q. Pan, J. Yao, Y.-M. You and R.-G. Xiong, Confinement-Driven Ferroelectricity in a Two-Dimensional Hybrid Lead Iodide Perovskite, *J. Am. Chem. Soc.*, 2020, **142**, 10212–10218.

16 W.-Q. Liao, Y. Zhang, C.-L. Hu, J.-G. Mao, H.-Y. Ye, P.-F. Li, S. D. Huang and R.-G. Xiong, A lead-halide perovskite molecular ferroelectric semiconductor, *Nat. Commun.*, 2015, **6**, 7338.

17 H. Ye, Y. Zhang, D. Fu and R. Xiong, An Above-Room-Temperature Ferroelectric Organo–Metal Halide Perovskite: (3-Pyrrolinium)(CdCl$_3$), *Angew. Chem.*, 2014, **126**, 11424–11429.

18 Y. Hou, C. Wu, D. Yang, T. Ye, V. G. Honavar, A. C. T. van Duin, K. Wang and S. Priya, Two-dimensional hybrid organic–inorganic perovskites as emergent ferroelectric materials, *J. Appl. Phys.*, 2020, **128**, 060906, DOI: 10.1063/5.0016010.

19 P. Zhao, J. Xu, C. Ma, W. Ren, L. Wang, L. Bian and A. Chang, Spontaneous polarization behaviors in hybrid halide perovskite film, *Scr. Mater.*, 2015, **102**, 51–54.

20 X.-G. Chen, X.-J. Song, Z.-X. Zhang, P.-F. Li, J.-Z. Ge, Y.-Y. Tang, J.-X. Gao, W.-Y. Zhang, D.-W. Fu, Y.-M. You and R.-G. Xiong, Two-Dimensional Layered Perovskite

This journal is © The Royal Society of Chemistry 2025

J. Mater. Chem. C, 2025, **13**, 10488–10506 | 10501

Ferroelectric with Giant Piezoelectric Voltage Coefficient, *J. Am. Chem. Soc.*, 2020, **142**, 1077–1082.

21 Z. Wu, C. Ji, L. Li, J. Kong, Z. Sun, S. Zhao, S. Wang, M. Hong and J. Luo, Alloying *n*-Butylamine into $CsPbBr_3$ To Give a Two-Dimensional Bilayered Perovskite Ferroelectric Material, *Angew. Chem., Int. Ed.*, 2018, **57**, 8140–8143.

22 Y. Zeng, X. Huang, C. Huang, H. Zhang, F. Wang and Z. Wang, Unprecedented 2D Homochiral Hybrid Lead-Iodide Perovskite Thermochromic Ferroelectrics with Ferroelastic Switching, *Angew. Chem., Int. Ed.*, 2021, **60**, 10730–10735.

23 M. M. Rana, A. A. Khan, W. Zhu, M. F. Al Fattah, S. Kokilathasan, S. Rassel, R. Bernard, S. Ababou-Girard, P. Turban, S. Xu, C. Wang and D. Ban, Enhanced piezoelectricity in lead-free halide perovskite nanocomposite for self-powered wireless electronics, *Nano Energy*, 2022, **101**, 107631.

24 V. Pecunia, S. R. P. Silva, J. D. Phillips, E. Artegiani, A. Romeo, H. Shim, J. Park, J. H. Kim, J. S. Yun, G. C. Welch, B. W. Larson, M. Creran, A. Laventure, K. Sasitharan, N. Flores-Diaz, M. Freitag, J. Xu, T. M. Brown, B. Li, Y. Wang, Z. Li, B. Hou, B. H. Hamadani, E. Defay, V. Kovacova, S. Glinsek, S. Kar-Narayan, Y. Bai, D. Bin Kim, Y. S. Cho, A. Žukauskaitė, S. Barth, F. R. Fan, W. Wu, P. Costa, J. del Campo, S. Lanceros-Mendez, H. Khanbareh, Z. L. Wang, X. Pu, C. Pan, R. Zhang, J. Xu, X. Zhao, Y. Zhou, G. Chen, T. Tat, I. W. Ock, J. Chen, S. A. Graham, J. S. Yu, L.-Z. Huang, D.-D. Li, M.-G. Ma, J. Luo, F. Jiang, P. S. Lee, B. Dudem, V. Vivekananthan, M. G. Kanatzidis, H. Xie, X.-L. Shi, Z.-G. Chen, A. Riss, M. Parzer, F. Garmroudi, E. Bauer, D. Zavanelli, M. K. Brod, M. Al Malki, G. J. Snyder, K. Kovnir, S. M. Kauzlarich, C. Uher, J. Lan, Y.-H. Lin, L. Fonseca, A. Morata, M. Martin-Gonzalez, G. Pennelli, D. Berthebaud, T. Mori, R. J. Quinn, J.-W. G. Bos, C. Candolfi, P. Gougeon, P. Gall, B. Lenoir, D. Venkateshvaran, B. Kaestner, Y. Zhao, G. Zhang, Y. Nonoguchi, B. C. Schroeder, E. Bilotti, A. K. Menon, J. J. Urban, O. Fenwick, C. Asker, A. A. Talin, T. D. Anthopoulos, T. Losi, F. Viola, M. Caironi, D. G. Georgiadou, L. Ding, L.-M. Peng, Z. Wang, M.-D. Wei, R. Negra, M. C. Lemme, M. Wagih, S. Beeby, T. Ibn-Mohammed, K. B. Mustapha and A. P. Joshi, Roadmap on energy harvesting materials, *J. Phys. Mater.*, 2023, **6**, 042501.

25 Y. Liu, D. Kim, A. V. Ievlev, S. V. Kalinin, M. Ahmadi and O. S. Ovchinnikova, Ferroic Halide Perovskite Optoelectronics, *Adv. Funct. Mater.*, 2021, **31**(36), 2102793, DOI: **10.1002/adfm.202102793**.

26 X. Chen, S. Cheng, L. Xiao and H. Sun, Identifying, understanding and controlling defects and traps in halide perovskites for optoelectronic devices: a review, *J. Phys. D: Appl. Phys.*, 2020, **53**, 373001.

27 J. Ye, M. M. Byranvand, C. O. Martínez, R. L. Z. Hoye, M. Saliba and L. Polavarapu, Defect Passivation in Lead-Halide Perovskite Nanocrystals and Thin Films: Toward Efficient LEDs and Solar Cells, *Angew. Chem.*, 2021, **133**, 21804–21828.

28 R. S. Muddam, S. Wang, N. P. Maria Joseph Raj, Q. Wang, P. Wijesinghe, J. Payne, M. S. Dyer, C. Bowen and L. Krishnan Jagadamma, Self-Poled Halide Perovskite Ruddlesden-Popper Ferroelectric-Photovoltaic Semiconductor Thin Films and Their Energy Harvesting Properties, *Adv. Funct. Mater.*, 2025, 2425192, DOI: **10.1002/adfm.202425192**.

29 F. U. Kosasih, E. Erdenebileg, N. Mathews, S. G. Mhaisalkar and A. Bruno, Thermal evaporation and hybrid deposition of perovskite solar cells and mini-modules, *Joule*, 2022, **6**, 2692–2734.

30 S. Siegrist, S.-C. Yang, E. Gilshtein, X. Sun, A. N. Tiwari and F. Fu, Triple-cation perovskite solar cells fabricated by a hybrid PVD/blade coating process using green solvents, *J. Mater. Chem. A*, 2021, **9**, 26680–26687.

31 D. Song, J. H. Heo, H. J. Han, M. S. You and S. H. Im, Reproducible formation of uniform $CH_3NH_3PbI_{3-x}Cl_x$ mixed halide perovskite film by separation of the powder formation and spin-coating process, *J. Power Sources*, 2016, **310**, 130–136.

32 *Ferroelectric Materials and Their Applications – Y. Xu – Google Books*, **https://books.google.co.uk/books?hl=en&lr=&id=dWkhBQAAQBAJ&oi=fnd&pg=PP1&dq=Inorganic+perovskite+ferroelectricity+origin+book&ots=8U9U25W4pl&sig=e7iqdJ4DWNtezg8UR2_tq8zgO8s#v=onepage&q&f=false**, (accessed 29 August 2024).

33 H. Zhu, T. Miyashita and M. Mitsuishi, Energy storage behaviors in ferroelectric capacitors fabricated with sub-50 nm poly(vinylidene fluoride) Langmuir–Blodgett nanofilms, *Polym. J.*, 2019, **51**, 795–801, DOI: **10.1038/s41428-019-0194-3**.

34 M. Stewart, M. G. Cain and D. Hall, *Ferroelectric Hysteresis Measurement & Analysis*, *NPL Report CMMT(A)152*, 1999, pp. 1–57.

35 I. H. Lone, J. Aslam, N. R. E. Radwan, A. H. Bashal, A. F. A. Ajlouni and A. Akhter, Multiferroic ABO_3 Transition Metal Oxides: a Rare Interaction of Ferroelectricity and Magnetism, *Nanoscale Res. Lett.*, 2019, **14**, 142.

36 V. Nagarajan, C. S. Ganpule, A. Roytburd and R. Ramesh, Nanoscale phenomena in ferroelectric thin films, *Integr. Ferroelectr.*, 2002, **42**(1), 173–189, DOI: **10.1080/10584580210862**.

37 Z. Fan, K. Sun and J. Wang, Perovskites for photovoltaics: a combined review of organic–inorganic halide perovskites and ferroelectric oxide perovskites, *J. Mater. Chem. A*, 2015, **3**, 18809–18828.

38 M. Bari, A. A. Bokov and Z.-G. Ye, Ferroelasticity, domain structures and phase symmetries in organic–inorganic hybrid perovskite methylammonium lead chloride, *J. Mater. Chem. C*, 2020, **8**, 9625–9631.

39 A. A. Bahgat, B. A. A. Makram, E. E. Shaisha and M. M. El-Desoky, Ferroelectricity in the glassy material of the composition Bi_2O_3–Pb_3O_4–CuO–K_2O, *J. Alloys Compd.*, 2010, **506**, 141–150.

40 C. H. Ahn, K. M. Rabe and J. M. Triscone, Ferroelectricity at the Nanoscale: Local Polarization in Oxide Thin Films and Heterostructures, *Science*, 2004, **303**(5657), 488–491, DOI: **10.1126/science.1092508**.

10502 | *J. Mater. Chem. C*, 2025, **13**, 10488–10506

This journal is © The Royal Society of Chemistry 2025

41 M. Mączka, A. Gagor, J. K. Zaręba, D. Stefanska, M. Drozd, S. Balciunas, M. Šimėnas, J. Banys and A. Sieradzki, Three-Dimensional Perovskite Methylhydrazinium Lead Chloride with Two Polar Phases and Unusual Second-Harmonic Generation Bistability above Room Temperature, *Chem. Mater.*, 2020, **32**, 4072–4082.

42 M. Mączka, M. Ptak, A. Gągor, D. Stefańska, J. K. Zaręba and A. Sieradzki, Methylhydrazinium Lead Bromide: Non-centrosymmetric Three-Dimensional Perovskite with Exceptionally Large Framework Distortion and Green Photoluminescence, *Chem. Mater.*, 2020, **32**, 1667–1673.

43 M. Mączka, M. Ptak, A. Gągor, J. K. Zaręba, X. Liang, S. Balčiūnas, O. A. Semenikhin, O. I. Kucheriv, I. A. Gural'skiy, S. Shova, A. Walsh, J. Banys and M. Šimėnas, Phase Transitions, Dielectric Response, and Nonlinear Optical Properties of Aziridinium Lead Halide Perovskites, *Chem. Mater.*, 2023, **35**, 9725–9738.

44 H. R. Petrosova, O. I. Kucheriv, S. Shova and I. A. Gural'skiy, Aziridinium cation templating 3D lead halide hybrid perovskites, *Chem. Commun.*, 2022, **58**, 5745–5748.

45 C. Ortiz-Cervantes, P. Carmona-Monroy and D. Solis-Ibarra, Two-Dimensional Halide Perovskites in Solar Cells: 2D or not 2D?, *ChemSusChem*, 2019, **12**, 1560–1575.

46 M. Mączka, J. K. Zaręba, A. Gągor, D. Stefańska, M. Ptak, K. Roleder, D. Kajewski, A. Soszyński, K. Fedoruk and A. Sieradzki, [Methylhydrazinium]$_2$PbBr$_4$, a Ferroelectric Hybrid Organic–Inorganic Perovskite with Multiple Non-linear Optical Outputs, *Chem. Mater.*, 2021, **33**, 2331–2342.

47 C. M. M. Soe, C. C. Stoumpos, M. Kepenekian, B. Traoré, H. Tsai, W. Nie, B. Wang, C. Katan, R. Seshadri, A. D. Mohite, J. Even, T. J. Marks and M. G. Kanatzidis, New Type of 2D Perovskites with Alternating Cations in the Interlayer Space, $(C(NH_2)_3)(CH_3NH_3)_nPb_nI_{3n+1}$: Structure, Properties, and Photovoltaic Performance, *J. Am. Chem. Soc.*, 2017, **139**, 16297–16309.

48 D. Drozdowski, K. Fedoruk, A. Kabanski, M. Maczka, A. Sieradzki and A. Gagor, Broadband yellow and white emission from large octahedral tilting in (110)-oriented layered perovskites: imidazolium-methylhydrazinium lead halides, *J. Mater. Chem. C*, 2023, **11**, 4907–4915.

49 Y.-Y. Guo, L.-J. Yang, S. Biberger, J. A. McNulty, T. Li, K. Schötz, F. Panzer and P. Lightfoot, Structural Diversity in Layered Hybrid Perovskites, A$_2$PbBr$_4$ or AA′PbBr$_4$, Templated by Small Disc-Shaped Amines, *Inorg. Chem.*, 2020, **59**, 12858–12866.

50 T. Niu, Q. Xue and H.-L. Yip, Advances in Dion-Jacobson phase two-dimensional metal halide perovskite solar cells, *Nanophotonics*, 2021, **10**, 2069–2102.

51 L. Mao, Y. Wu, C. C. Stoumpos, B. Traore, C. Katan, J. Even, M. R. Wasielewski and M. G. Kanatzidis, Tunable White-Light Emission in Single-Cation-Templated Three-Layered 2D Perovskites $(CH_3CH_2NH_3)_4Pb_3Br_{10-x}Cl_x$, *J. Am. Chem. Soc.*, 2017, **139**, 11956–11963.

52 A. García-Fernández, J. M. Bermúdez-García, S. Castro-García, A. L. Llamas-Saiz, R. Artiaga, J. J. López-Beceiro, M. Sánchez-Andújar and M. A. Señarís-Rodríguez,

$[(CH_3)_2NH_2]_7Pb_4X_{15}$ (X = Cl$^-$ and Br$^-$), 2D-Perovskite Related Hybrids with Dielectric Transitions and Broadband Photoluminiscent Emission, *Inorg. Chem.*, 2018, **57**, 3215–3222.

53 C. C. Stoumpos, L. Mao, C. D. Malliakas and M. G. Kanatzidis, Structure–Band Gap Relationships in Hexagonal Polytypes and Low-Dimensional Structures of Hybrid Tin Iodide Perovskites, *Inorg. Chem.*, 2017, **56**, 56–73.

54 M. A. Green, A. Ho-Baillie and H. J. Snaith, The emergence of perovskite solar cells, *Nat. Photonics*, 2014, **8**, 506–514.

55 S. Yu, P. Liu and S. Xiao, A review of main characterization methods for identifying two-dimensional organic–inorganic halide perovskites, *J. Mater. Sci.*, 2021, **56**, 11656–11681, DOI: **10.1007/s10853-021-06038-2**.

56 M. Mączka, J. K. Zaręba, A. Gągor, K. Fedoruk-Piskorska, D. Stefańska, D. Drozdowski, M. Ptak and A. Sieradzki, Multi-Noncentrosymmetric Polar Order in 2D Hybrid Lead Chloride with Broadband Emission and High-Temperature Second-Harmonic Generation Switching, *ACS Appl. Mater. Interfaces*, 2024, **16**, 60564–60575.

57 X.-G. Chen, X.-J. Song, Z.-X. Zhang, P.-F. Li, J.-Z. Ge, Y.-Y. Tang, J.-X. Gao, W.-Y. Zhang, D.-W. Fu, Y.-M. You and R.-G. Xiong, Two-Dimensional Layered Perovskite Ferroelectric with Giant Piezoelectric Voltage Coefficient, *J. Am. Chem. Soc.*, 2020, **142**, 1077–1082.

58 H. Ye, W. Liao, C. Hu, Y. Zhang, Y. You, J. Mao, P. Li and R. Xiong, Bandgap Engineering of Lead-Halide Perovskite-Type Ferroelectrics, *Adv. Mater.*, 2016, **28**, 2579–2586.

59 C. Ji, S. Wang, L. Li, Z. Sun, M. Hong and J. Luo, The First 2D Hybrid Perovskite Ferroelectric Showing Broadband White-Light Emission with High Color Rendering Index, *Adv. Funct. Mater.*, 2019, **29**(6), 1805038, DOI: **10.1002/adfm.201805038**.

60 P.-P. Shi, S.-Q. Lu, X.-J. Song, X.-G. Chen, W.-Q. Liao, P.-F. Li, Y.-Y. Tang and R.-G. Xiong, Two-Dimensional Organic–Inorganic Perovskite Ferroelectric Semiconductors with Fluorinated Aromatic Spacers, *J. Am. Chem. Soc.*, 2019, **141**, 18334–18340.

61 X. Liu, Z. Wu, T. Guan, H. Jiang, P. Long, X. Li, C. Ji, S. Chen, Z. Sun and J. Luo, Giant room temperature electrocaloric effect in a layered hybrid perovskite ferroelectric: $[(CH_3)_2CHCH_2NH_3]_2PbCl_4$, *Nat. Commun.*, 2021, **12**, 5502.

62 N. Wang, N. Ding, Z. Xu, W. Luo, H. Li, C. Shi, H. Ye, S. Dong and L. Miao, Large Enhancement of Polarization in a Layered Hybrid Perovskite Ferroelectric Semiconductor via Molecular Engineering, *Small*, 2024, **20**(10), 2306502, DOI: **10.1002/smll.202306502.**

63 C. Ji, D. Dey, Y. Peng, X. Liu, L. Li and J. Luo, Ferroelectricity-Driven Self-Powered Ultraviolet Photodetection with Strong Polarization Sensitivity in a Two-Dimensional Halide Hybrid Perovskite, *Angew. Chem.*, 2020, **132**, 19095–19099.

64 H.-Y. Zhang, Z.-X. Zhang, X.-J. Song, X.-G. Chen and R.-G. Xiong, Two-Dimensional Hybrid Perovskite Ferroelectric

This journal is © The Royal Society of Chemistry 2025

J. Mater. Chem. C, 2025, **13**, 10488–10506 | **10503**

Induced by Perfluorinated Substitution, *J. Am. Chem. Soc.*, 2020, **142**, 20208–20215.

65 Q.-Q. Jia, G. Teri, J.-Q. Luo, H.-F. Ni, P.-Z. Huang, M.-M. Lun, Z.-X. Zhang, Y. Zhang and D.-W. Fu, Experimental Observation of the Fully Ferroelectric–Fully Ferroelastic Effect in Multiferroic Hybrid Perovskites, *J. Am. Chem. Soc.*, 2024, **146**, 21120–21128.

66 Y. Ma, B. Wang, W. Li, Y. Liu, W. Guo, H. Xu, L. Tang, Q. Fan, J. Luo and Z. Sun, Unusual Triple-State Switching of Thermally Induced Birefringence in a Two-Dimensional Perovskite Ferroelectric, *J. Am. Chem. Soc.*, 2024, **146**, 27287–27292.

67 W. He, Y. Yang, C. Li, W. P. D. Wong, F. Cimpoesu, A. M. Toader, Z. Wu, X. Wu, Z. Lin, Q. Xu, K. Leng, A. Stroppa and K. P. Loh, Near-90° Switch in the Polar Axis of Dion–Jacobson Perovskites by Halide Substitution, *J. Am. Chem. Soc.*, 2023, **145**, 14044–14051.

68 C.-C. Fan, C.-D. Liu, B.-D. Liang, M.-L. Jin, T.-Y. Ju, C.-Y. Chai, X.-B. Han and W. Zhang, A Two-Dimensional Hybrid Lead Bromide Ferroelectric Semiconductor with an Out-of-Plane Polarization, *Inorg. Chem.*, 2023, **62**, 12634–12638.

69 H.-Y. Zhang, Z.-X. Zhang, X.-G. Chen, X.-J. Song, Y. Zhang and R.-G. Xiong, Large Electrostrictive Coefficient in a Two-Dimensional Hybrid Perovskite Ferroelectric, *J. Am. Chem. Soc.*, 2021, **143**, 1664–1672.

70 Z. Wu, C. Ji, L. Li, J. Kong, Z. Sun, S. Zhao, S. Wang, M. Hong and J. Luo, Alloying *n*-Butylamine into CsPbBr₃ To Give a Two-Dimensional Bilayered Perovskite Ferroelectric Material, *Angew. Chem., Int. Ed.*, 2018, **57**, 8140–8143.

71 Y. Ma, W. Li, J. Sun, Y. Liu, W. Guo, H. Rong, Q. Li, X. Fu, J. Luo and Z. Sun, Unlocking Cage-Confined Cations Molecular Dynamics toward High-*T*c Perovskite Ferroelectrics, *Angew. Chem.*, 2025, **64**(8), e202420512, DOI: **10.1002/ange.202420512**.

72 Y. Ma, W. Li, Y. Liu, W. Guo, H. Xu, L. Tang, Q. Fan, H. Rong, J. Luo and Z. Sun, Precise Tailoring of Unprecedent Layered Perovskite-Type Heterostructure Ferroelectric via Chemical Molecular Scissor, *Angew. Chem.*, 2025, **64**(9), e202424279, DOI: **10.1002/anie.202424279**.

73 K. Li, F. Wu, X. Li, B. Li, Z. Sun, X. Wang, X. Liu and J. Luo, Self-Powered Filterless Narrowband UV Photodetection Triggered by Asymmetric Charge Carrier Generation in a Wide-Bandgap Halide Perovskite Ferroelectric, *Small*, 2025, **21**(8), 2409544, DOI: **10.1002/smll.202409544**.

74 Y. Ma, J. Wang, W. Guo, S. Han, J. Xu, Y. Liu, L. Lu, Z. Xie, J. Luo and Z. Sun, The First Improper Ferroelectric of 2D Multilayered Hybrid Perovskite Enabling Strong Tunable Polarization-Directed Second Harmonic Generation Effect, *Adv. Funct. Mater.*, 2021, **31**(37), 2103012, DOI: **10.1002/adfm.202103012**.

75 Y. Jiang, C. Zhang, Z. Zhu, J. Wu, P. Yu, Y. Zeng, H. Ye, H. Dai, R. Li, Q. Guan, G. Chen, H. Yang and J. Luo, Multi-Axial Self-Driven X-Ray Detection by a Two-Dimensional Biaxial Hybrid Organic-Inorganic Perovskite Ferroelectric, *Angew. Chem., Int. Ed.*, 2024, **63**(44), e202407305, DOI: **10.1002/anie.202407305**.

76 L. Li, X. Liu, Y. Li, Z. Xu, S. Wu, S. Han, K. Tao, M. Hong, J. Luo and Z. Sun, Two-Dimensional Hybrid Perovskite-Type Ferroelectric for Highly Polarization-Sensitive Short-wave Photodetection, *J. Am. Chem. Soc.*, 2019, **141**, 2623–2629.

77 C. Ji, S. Wang, Y. Wang, H. Chen, L. Li, Z. Sun, Y. Sui, S. Wang and J. Luo, 2D Hybrid Perovskite Ferroelectric Enables Highly Sensitive X-Ray Detection with Low Driving Voltage, *Adv. Funct. Mater.*, 2020, **30**(5), 1905529, DOI: **10.1002/adfm.201905529**.

78 Y. Peng, J. Bie, X. Liu, L. Li, S. Chen, W. Fa, S. Wang, Z. Sun and J. Luo, Acquiring High-*T*c Layered Metal Halide Ferroelectrics via Cage-Confined Ethylamine Rotators, *Angew. Chem., Int. Ed.*, 2021, **60**, 2839–2843.

79 X. Li, F. Wu, Y. Yao, W. Wu, C. Ji, L. Li, Z. Sun, J. Luo and X. Liu, Robust Spin-Dependent Anisotropy of Circularly Polarized Light Detection from Achiral Layered Hybrid Perovskite Ferroelectric Crystals, *J. Am. Chem. Soc.*, 2022, **144**, 14031–14036.

80 Y. Ma, W. Li, Y. Liu, W. Guo, H. Xu, S. Han, L. Tang, Q. Fan, J. Luo and Z. Sun, Mixing cage cations in 2D metal-halide ferroelectrics enhances the ferro-pyro-phototronic effect for self-driven photopyroelectric detection, *Chem. Sci.*, 2023, **14**, 10347–10352.

81 H. Ye, Y. Peng, X. Shang, L. Li, Y. Yao, X. Zhang, T. Zhu, X. Liu, X. Chen and J. Luo, Self-Powered Visible-Infrared Polarization Photodetection Driven by Ferroelectric Photovoltaic Effect in a Dion–Jacobson Hybrid Perovskite, *Adv. Funct. Mater.*, 2022, **32**(24), 2200223, DOI: **10.1002/adfm.202200223**.

82 Z. Fan, K. Sun and J. Wang, Perovskites for photovoltaics: a combined review of organic-inorganic halide perovskites and ferroelectric oxide perovskites, *J. Mater. Chem. A*, 2015, (3), 18809–18828.

83 J. García-Ben, A. García-Fernández, P. Dafonte-Rodríguez, I. Delgado-Ferreiro, U. B. Cappel, S. Castro-García, M. Sánchez-Andújar, J. M. Bermúdez-García and M. A. Señarís-Rodríguez, Narrowing the tolerance factor limits for hybrid organic-inorganic dicyanamide-perovskites, *J. Solid State Chem.*, 2022, **316**, 123635.

84 G. Kieslich, S. Sun and A. K. Cheetham, An extended Tolerance Factor approach for organic–inorganic perovskites, *Chem. Sci.*, 2015, **6**, 3430–3433.

85 J. García-Ben, A. García-Fernández, P. Dafonte-Rodríguez, I. Delgado-Ferreiro, U. B. Cappel, S. Castro-García, M. Sánchez-Andújar, J. M. Bermúdez-García and M. A. Señarís-Rodríguez, Narrowing the tolerance factor limits for hybrid organic-inorganic dicyanamide-perovskites, *J. Solid State Chem.*, 2022, **316**, 123635.

86 M. Mączka, M. Ptak, A. Gągor, D. Stefańska, J. K. Zaręba and A. Sieradzki, Methylhydrazinium Lead Bromide: Non-centrosymmetric Three-Dimensional Perovskite with Exceptionally Large Framework Distortion and Green Photoluminescence, *Chem. Mater.*, 2020, **32**, 1667–1673.

10504 | *J. Mater. Chem. C*, 2025, **13**, 10488–10506

This journal is © The Royal Society of Chemistry 2025

87 M. I. Bodnarchuk, L. G. Feld, C. Zhu, S. C. Boehme, F. Bertolotti, J. Avaro, M. Aebli, S. H. Mir, N. Masciocchi, R. Erni, S. Chakraborty, A. Guagliardi, G. Rainò and M. V. Kovalenko, Colloidal Aziridinium Lead Bromide Quantum Dots, *ACS Nano*, 2024, **18**(7), 5684–5697, DOI: **10.1021/acsnano.3c11579**.

88 S. Gholipour, A. M. Ali, J. Correa-Baena, S. Turren-Cruz, F. Tajabadi, W. Tress, N. Taghavinia, M. Grätzel, A. Abate, F. De Angelis, C. A. Gaggioli, E. Mosconi, A. Hagfeldt and M. Saliba, Globularity-Selected Large Molecules for a New Generation of Multication Perovskites, *Adv. Mater.*, 2017, **29**(38), 1702005, DOI: **10.1002/adma.201702005**.

89 J. García-Ben, A. García-Fernández, P. Dafonte-Rodríguez, I. Delgado-Ferreiro, U. B. Cappel, S. Castro-García, M. Sánchez-Andújar, J. M. Bermúdez-García and M. A. Señarís-Rodríguez, Narrowing the tolerance factor limits for hybrid organic-inorganic dicyanamide-perovskites, *J. Solid State Chem.*, 2022, **316**, 123635.

90 S. Burger, M. G. Ehrenreich and G. Kieslich, Tolerance factors of hybrid organic–inorganic perovskites: recent improvements and current state of research, *J. Mater. Chem. A*, 2018, **6**, 21785–21793.

91 J. Bin Li, Z. K. Jiang, R. Wang, J. Z. Zhao and R. Wang, Ferroelectric order in hybrid organic-inorganic perovskite NH_4PbI_3 with non-polar molecules and small tolerance factor, *NPJ Comput. Mater.*, 2023, **9**, 62, DOI: **10.1038/s41524-023-01019-2**.

92 G. Giorgi, J.-I. Fujisawa, H. Segawa and K. Yamashita, Organic–Inorganic Hybrid Lead Iodide Perovskite Featuring Zero Dipole Moment Guanidinium Cations: A Theoretical Analysis, *J. Phys. Chem. C*, 2015, **119**, 4694–4701.

93 F. B. Minussi and E. B. Araújo, On the prospects of high-entropy organic A-site halide perovskites, *Phys. Chem. Chem. Phys.*, 2024, **26**, 26479–26488.

94 Y. Yang, W. Ren, M. Stengel, X. H. Yan and L. Bellaiche, Revisiting Properties of Ferroelectric and Multiferroic Thin Films under Tensile Strain from First Principles, *Phys. Rev. Lett.*, 2012, **109**, 057602.

95 S. Tominaka, I. Karimata, T. Matsuoka, M. Sakamoto, T. Nakajima, K. Ohara and T. Tachikawa, Dynamic Symmetry Conversion in Mixed-Halide Hybrid Perovskite upon Illumination, *ACS Energy Lett.*, 2021, **6**, 3858–3863.

96 Z. Fan, J. Xiao, K. Sun, L. Chen, Y. Hu, J. Ouyang, K. P. Ong, K. Zeng and J. Wang, Ferroelectricity of $CH_3NH_3PbI_3$ Perovskite, *J. Phys. Chem. Lett.*, 2015, **6**, 1155–1161.

97 L. Li, X. Liu, Y. Li, Z. Xu, Z. Wu, S. Han, K. Tao, M. Hong, J. Luo and Z. Sun, Two-Dimensional Hybrid Perovskite-Type Ferroelectric for Highly Polarization-Sensitive Shortwave Photodetection, *J. Am. Chem. Soc.*, 2019, **141**, 2623–2629.

98 J. M. Bermúdez-García, A. García-Fernández, A. Andrada-Chacón, J. Sánchez-Benítez, W. Ren, S. Hu, T. Gu, H. Xiang, M. Biczysko, S. Castro-García, M. Sánchez-Andújar, A. Stroppa and M. A. Señarís-Rodríguez, Pressure-induced reversible framework rearrangement and increased polarization in the polar $[NH_4][Cd(HCOO)_3]$ hybrid perovskite, *Inorg. Chem. Front.*, 2019, **6**, 2379–2386.

99 J.-H. Lee, A. Jaffe, Y. Lin, H. I. Karunadasa and J. B. Neaton, Origins of the Pressure-Induced Phase Transition and Metallization in the Halide Perovskite (CH_3NH_3)PbI_3, *ACS Energy Lett.*, 2020, **5**, 2174–2181.

100 S. Sobczak, A. Nowok, J. K. Zaręba, K. Roszak, A. Półrolniczak, A. Z. Szeremeta, B. Dziuk, F. Dybała, S. Pawlus, R. Kudrawiec, A. Sieradzki, M. Mączka and A. Katrusiak, Expanding the horizons of the thermodynamic landscape and optoelectronic properties of soft 2D hybrid perovskites MHy_2PbX_4, *J. Mater. Chem. A*, 2024, **12**, 16803–16814.

101 S. Zhang, S.-M. Lee, D.-H. Kim, H.-Y. Lee and T. R. Shrout, Temperature dependence of the dielectric, piezoelectric, and elastic constants for $Pb(Mg_{1/3}Nb_{2/3})O_3–PbZrO_3–PbTiO_3$ piezocrystals, *J. Appl. Phys.*, 2007, **102**, 114103, DOI: **10.1063/1.2817641**.

102 M. Li, H. J. Wondergem, M.-J. Spijkman, K. Asadi, I. Katsouras, P. W. M. Blom and D. M. de Leeuw, Revisiting the δ-phase of poly(vinylidene fluoride) for solution-processed ferroelectric thin films, *Nat. Mater.*, 2013, **12**, 433–438.

103 S. Picozzi, Ferroelectric Rashba semiconductors as a novel class of multifunctional materials, *Front. Phys.*, 2014, **2**, 10, DOI: **10.3389/fphy.2014.00010**.

104 I.-H. Park, Q. Zhang, K. C. Kwon, Z. Zhu, W. Yu, K. Leng, D. Giovanni, H. S. Choi, I. Abdelwahab, Q.-H. Xu, T. C. Sum and K. P. Loh, Ferroelectricity and Rashba Effect in a Two-Dimensional Dion-Jacobson Hybrid Organic–Inorganic Perovskite, *J. Am. Chem. Soc.*, 2019, **141**, 15972–15976.

105 Y. Ma, W. Li, Y. Liu, W. Guo, H. Xu, L. Tang, Q. Fan, H. Rong, J. Luo and Z. Sun, Precise Tailoring of Unprecedent Layered Perovskite-Type Heterostructure Ferroelectric via Chemical Molecular Scissor, *Angew. Chem.*, 2025, **137**(9), e202424279, DOI: **10.1002/ange.202424279**.

106 A. Pishtshev and E. Strugovshchikov, Discovering Ferro- and Piezoelectricity in Lead-Free Oxyhydrides Ln_2H_4O (Ln = Y, La), *Adv. Theory Simul.*, 2019, **2**(12), 1900144, DOI: **10.1002/adts.201900144**.

107 N. Fathalizadeh, S. Shojaei and S. Ahmadi-Kandjani, Electronic and optical properties of two-dimensional perovskite materials in DJ and RP phases: density functional theory approach, *Opt. Quantum Electron.*, 2023, **55**, 950.

108 Q. Zhang, A. Solanki, K. Parida, D. Giovanni, M. Li, T. L. C. Jansen, M. S. Pshenichnikov and T. C. Sum, Tunable Ferroelectricity in Ruddlesden–Popper Halide Perovskites, *ACS Appl. Mater. Interfaces*, 2019, **11**, 13523–13532.

109 R. Sekhar Muddam, J. Sinclair and L. Krishnan Jagadamma, Piezoelectric Charge Coefficient of Halide Perovskites, *Materials*, 2024, **17**, 3083.

110 B. Han, Y. Wang, C. Liu, K. Sun, M. Yang, L. Xie, S. Yang, Y. Meng, S. Lin, P. Xu, J. Li, Q. Qiu and Z. Ge, Rational Design of Ferroelectric 2D Perovskite for Improving the Efficiency of Flexible Perovskite Solar Cells Over 23%, *Angew. Chem., Int. Ed.*, 2023, **62**(8), e202217526, DOI: **10.1002/anie.202217526**.

This journal is © The Royal Society of Chemistry 2025

J. Mater. Chem. C, 2025, **13**, 10488–10506 | **10505**

111 N. Phung, A. Al-Ashouri, S. Meloni, A. Mattoni, S. Albrecht, E. L. Unger, A. Merdasa and A. Abate, The Role of Grain Boundaries on Ionic Defect Migration in Metal Halide Perovskites, *Adv. Energy Mater.*, 2020, **10**(20), 1903735, DOI: **10.1002/aenm.201903735**.

112 R. Ding, Y. Lyu, Z. Wu, F. Guo, W. F. Io, S. Pang, Y. Zhao, J. Mao, M. Wong and J. Hao, Effective Piezo-Phototronic Enhancement of Flexible Photodetectors Based on 2D Hybrid Perovskite Ferroelectric Single-Crystalline Thin-Films, *Adv. Mater.*, 2021, **33**(32), 2101263, DOI: **10.1002/adma.202101263**.

113 H. Xu, F. Sun, W. Guo, S. Han, Y. Liu, Q. Fan, L. Tang, W. Liu, J. Luo and Z. Sun, Building Block-Inspired Hybrid Perovskite Derivatives for Ferroelectric Channel Layers with Gate-Tunable Memory Behavior, *Angew. Chem., Int. Ed.*, 2023, **62**(45), e202309416, DOI: **10.1002/anie.202309416**.

10506 | *J. Mater. Chem. C*, 2025, **13**, 10488–10506

This journal is © The Royal Society of Chemistry 2025